LAWRENCE
LIVERMORE
NATIONAL
LABORATORY

LLNL-JRNL-846488

Computational design of metamaterials with self contact

A. Dalklint, F. Sjovall, M. Wallin, S. Watts, D. A. Tortorelli

March 19, 2023

Computer Methods in Applied Mechanics and Engineering

Disclaimer

This document was prepared as an account of work sponsored by an agency of the United States government. Neither the United States government nor Lawrence Livermore National Security, LLC, nor any of their employees makes any warranty, expressed or implied, or assumes any legal liability or responsibility for the accuracy, completeness, or usefulness of any information, apparatus, product, or process disclosed, or represents that its use would not infringe privately owned rights. Reference herein to any specific commercial product, process, or service by trade name, trademark, manufacturer, or otherwise does not necessarily constitute or imply its endorsement, recommendation, or favoring by the United States government or Lawrence Livermore National Security, LLC. The views and opinions of authors expressed herein do not necessarily state or reflect those of the United States government or Lawrence Livermore National Security, LLC, and shall not be used for advertising or product endorsement purposes.

LLNL-JRNL-846488

Computational design of metamaterials with self contact

Anna Dalklint[a,*], Filip Sjövall[a], Mathias Wallin[a], Seth Watts[b], Daniel Tortorelli[b,c]

[a] *Division of Solid Mechanics, Lund University, Box 118, SE-22100 Lund, Sweden.*
[b] *Center for Design and Optimization, Lawrence Livermore National Laboratory, Livermore, CA, USA*
[c] *Department of Mechanical Science and Engineering, University of Illinois at Urbana-Champaign, Urbana, Illinois, USA*

Abstract

Inverse homogenization in combination with contact modeling, topology optimization and shape optimization is used to design metamaterials with optimized macroscopic response. The homogenization assumes length scale separation which allows the non-linear macroscopic behavior to be obtained by analyzing a single unit cell in a lattice structure. Self contact in the unit cell, which is modeled using a third medium contact method, is leveraged to obtain a complex homogenized response. The inverse homogenization problem is initially formulated as a topology optimization problem, where the macroscopic stress-strain behavior is tuned to our liking. However, it is well known that boundary phenomena are difficult to model in topology optimization and that interface modeling is crucial to accurately analyze contact. For that reason, the boundary representation of the topology optimized design is extracted and used as initial design in a subsequent shape optimization. The behaviors of our designs are verified by performing rigorous post-processing analyzes using conforming meshes and conventional contact formulations.

Keywords: Topology optimization, Shape optimization, Internal contact, Third medium contact method, Tunable material properties, Finite strain

1. Introduction

Novel materials with tailored macroscopic properties can be realized via the ingenious design of their underlying microstructure. These engineered materials are often labeled *metamaterials*, and may possess extraordinary properties such as negative Poisson's ratio (Lakes [29], Evans and Alderson [21]), negative thermal expansion (Lakes [30], Wang et al. [56]) and negative refractive index (Zhang et al. [60], Valentine et al. [47]).

In contrast to the experimental or heuristic driven design approaches used in the aforementioned studies, there also exist systematic methods that use non-linear programming to design metamaterials. These *inverse homogenization* design problems can be solved with topology optimization. Indeed, we find a multitude of examples where topology optimization has been applied to design metamaterials with the previously mentioned properties (Wang et al. [54], Clausen et al. [14], Wang [52], Wallin and Tortorelli [51], Sigmund and Torquato [40], Sigmund [37], Christiansen and Sigmund [13]). Other interesting applications of inverse homogenization include maximum energy dissipation materials (Chen et al. [11], Ivarsson

*Corresponding author. E-mail adress: anna.dalklint@solid.lth.se

et al. [27], Deng et al. [20], Zhang and Khandelwal [59]) and maximum phononic/photonic bandgap materials (Sigmund and Jensen [38], Swartz et al. [46], Dalklint et al. [17]).

Various non-linear mechanisms can be exploited to tailor the macroscopic properties of a metamaterial. For example, Chen et al. [11] and Deng et al. [20] utilize snap-through to maximize the energy dissipation of hyperelastic materials. Bertoldi and Boyce [4] and Wang et al. [55] use buckling to tune phononic bandgaps. Irreversible processes are used to maximize energy dissipation via elastoplasticity (Alberdi and Khandelwal [1]) and viscoplasticity (Ivarsson et al. [27]).

Contact is another non-linear phenomena which has previously been considered in the topology optimization of macroscopic structures (Strömberg and Klarbring [42], Fernandez et al. [22]). Self-contact is exploited by Coulais et al. [15] and Wagner et al. [49] to heuristically design tunable-stiffness metamaterials. However, to the authors' knowledge, the modeling of self-contact in the inverse homogenization of metamaterials has only been briefly addressed by Bluhm [6].

Contact is rarely included in a topology optimization framework due to its inherent complexity. This issue was recently addressed by Bluhm et al. [7], by using the so-called *third medium* contact method. This contact formulation was pioneered by Wriggers et al. [57], and is conducive to density-based topology optimization, since the contact modeling third medium is the topology optimization ersatz void material, cf. Bluhm et al. [7] and Bluhm [6]. Although the third medium method is not as accurate as other contact models, and cannot model friction, it appears to produce reasonable designs. Inspired by this work, we use the third medium approach in our inverse homogenization study.

It is well known that boundary effects are not accurately modeled in topology optimization. To remedy this, we use the topology optimized designs as initial designs in a subsequent shape optimization framework. Unfortunately, we have no CAD representation of our topology optimized design, which complicates the shape optimization. However, mimicking the volume fraction field that dictates the topology optimization design, a design displacement field dictates the shape optimization design. This displacement morphs the initial topology optimized design into the shape optimized design. Upon discretization, we have nodal design displacement vectors that we "shape" optimize, just as we have element volume fractions that we "topology" optimize.

One of the earliest approaches to shape optimization via nodal coordinates was presented in Zienkiewicz and Campbell [61]. Unfortunately, this approach leads to ill-posed optimization problems (Chenais [12]), which give rise to solutions with infinitely fine oscillating boundaries and numerical artifacts such as "zig-zag" boundaries and inverted elements (Zienkiewicz and Campbell [61]). The analogous issue arises in density-based topology optimization using SIMP, where the "optimal" design contains non-converging distributions of smaller and smaller holes, i.e. no optimal solution exist (Bendsøe [3], Sigmund and Petersson [39]). In topology optimization, a well-posed optimization problem can be obtained by for example restricting the design space via sensitivity filtering (Sigmund [37]), perimeter constraints (Haber et al. [24], Amstutz and Van Goethem [2]) or design field filtering (Bruns and Tortorelli [10], Lazarov and Sigmund [31]). The latter approach can also be used to formulate a well-posed shape optimization problem, as exemplified by Le et al. [32] and Bletzinger [5]. A similar effect is obtained by Scherer et al. [36], wherein the filtered design displacement field is the solution to a non-linear hyperelasticity boundary-value problem. This is similar in spirit to the PDE filter used in topology optimization, cf. Lazarov and Sigmund [31]. In Scherer et al. [36] the design displacement field is applied as a Dirichlet boundary condition to the structure

that is being shape optimized. The filter analysis uses a hyperelastic energy function which is insensitive to rotations, translations and dilations, but sensitive to shearing and stretching. In this way, the quality of the morphed finite element mesh is maintained. To further enhance the mesh quality, they enforce an upper bound on the total "filter" energy. We follow Scherer et al. [36], however we replace the Dirichlet boundary conditions with Robin boundary conditions. This can be viewed as the shape optimization equivalent of the PDE filter introduced by Wallin et al. [50] in topology optimization.

Summarizing, in this study, we use a density based topology optimization to design hyperelastic metamaterials with prescribed macroscopic stress-strain response. To evaluate the homogenized response, we assume separation of length scales in the micro-to-macro transition to limit the analysis to a single unit cell, and enforce the periodic boundary conditions via Lagrange multipliers. Complex non-linear macroscopic material behavior is accomplished through self-contact within the unit cell, which is modeled via the third medium formulation. The topology optimized design is improved by using it as the initial design in a shape optimization wherein the contact is again modeled via the third medium approach. The numerical analysis is based on a standard finite element framework. To solve the optimization problems, we employ the gradient based method MMA (Method of Moving Asymptotes, cf. Svanberg [43]) and use the adjoint method to compute the gradients. Our designs are validated by performing rigorous post-processing analyzes in which the shape optimized designs are analyzed via a conventional contact formulation.

2. Governing equations

We consider the two-dimensional macroscopic body in its undeformed configuration $\Omega^M \in \mathbb{R}^2$, which consists of a lattice material with periodic microstructure, cf. Fig. 1. The material response at each macroscopic material point $\boldsymbol{X}^M \in \Omega^M$ is characterized by homogenizing the local response of the unit cell $\Omega(\boldsymbol{X}^M) \in \mathbb{R}^2$, under the assumption of separation of length scales, wherefore $|\Omega| \ll |\Omega^M|$, where $|\cdot|$ denotes the area[1]. Without loss of generality, we consider square unit cells centered at the origin with lattice vectors $\boldsymbol{A}_1 = a\boldsymbol{e}_1$ and $\boldsymbol{A}_2 = a\boldsymbol{e}_2$, where $\boldsymbol{e}_1$ and $\boldsymbol{e}_2$ are the standard 2D orthonormal basis vectors and $a > 0$. The unit cell boundary $\partial\Omega$ with outward unit normal $\boldsymbol{n}$ is decomposed into the complementary sets $\partial\Omega^+ = \partial\Omega^{1+} \cup \partial\Omega^{2+}$ and $\partial\Omega^- = \partial\Omega^{1-} \cup \partial\Omega^{2-}$, containing material points on opposite boundaries.

When loaded, the macroscopic body is deformed into the current equilibrium configuration, $\Omega_c^M \in \mathbb{R}^2$. The transformation is described by a smooth mapping $\boldsymbol{\varphi}^M : \Omega^M \to \Omega_c^M$, from which we extract the macroscopic deformation gradient, $\boldsymbol{F}^M = \boldsymbol{\nabla}^M \boldsymbol{\varphi}^M$, where $\boldsymbol{\nabla}^M$ is the gradient operator with respect to the macroscopic reference location $\boldsymbol{X}^M$. The macroscopic deformation $\boldsymbol{F}^M$ drives the unit cell microscopic displacement field $\boldsymbol{u} : \Omega \to \mathbb{R}^2$, such that each microscopic material point $\boldsymbol{X} \in \Omega$, is displaced to the position $\boldsymbol{x} = \boldsymbol{u}(\boldsymbol{X}) + \boldsymbol{X} \in \Omega_c$, where

$$\boldsymbol{u}(\boldsymbol{X}) = \left(\boldsymbol{F}^M\left(\boldsymbol{X}^M\right) - \boldsymbol{1}\right)\boldsymbol{X} + \boldsymbol{u}^F(\boldsymbol{X}), \quad \boldsymbol{X} \in \Omega, \tag{1}$$

and $\boldsymbol{u}^F : \Omega \to \mathbb{R}^2$ is the fluctuation displacement field, cf. Saeb et al. [35]. The microscopic

[1]Subsequently, we employ the $(\cdot)^M$ notation for all macroscopic quantities, and the $(\cdot)$ notation for microscopic quantities.

deformation gradient $\boldsymbol{F}$ is derived from (1) as

$$\boldsymbol{F}(\boldsymbol{X}) = \mathbf{1} + \boldsymbol{\nabla}\boldsymbol{u}(\boldsymbol{X}) = \boldsymbol{F}^M\left(\boldsymbol{X}^M\right) + \boldsymbol{\nabla}\boldsymbol{u}^F(\boldsymbol{X}), \quad \boldsymbol{X} \in \Omega, \tag{2}$$

where $\boldsymbol{F}^M$ is uniform over Ω due to the separation of scales and $\boldsymbol{\nabla}$ is the gradient operator with respect to the microscopic reference coordinates $\boldsymbol{X}$. For future convenience, we denote $J = \det\boldsymbol{F}$.

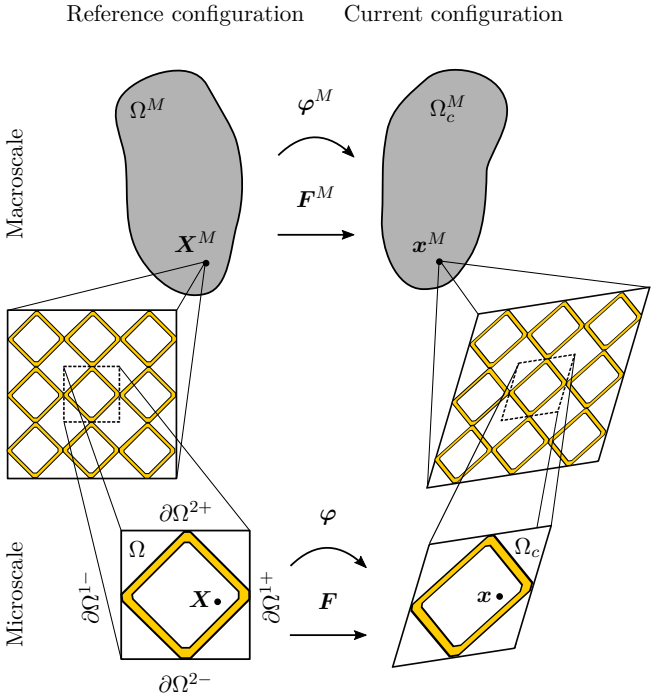

Fig. 1. The deformation of a macroscopic body and its effect on the periodic microstructure.

2.1. Micro-macro relations

To maintain consistency in the micro-to-macro transition, the variational form of the Hill-Mandel condition (Hill [26], Mandel [34]), which relates the virtual work due to the macroscopic first Piola-Kirchhoff stress $\boldsymbol{P}^M$ to the virtual work due to its microscopic counterpart $\boldsymbol{P}$, must be satisfied[2]

$$|\Omega|\delta\boldsymbol{F}^M\left(\boldsymbol{X}^M\right) : \boldsymbol{P}^M\left(\boldsymbol{X}^M\right) = \int_\Omega \delta\boldsymbol{F}(\boldsymbol{X}) : \boldsymbol{P}(\boldsymbol{X})\, dV, \tag{3}$$

where our hyperelastic assumption necessitates that $\boldsymbol{P} = \frac{\partial W}{\partial \boldsymbol{F}}$ where W is the microscopic energy function. In (3), $\delta\boldsymbol{u}$ is the kinematically admissible smooth virtual displacement that satisfies the kinematic consistency conditions $\int_\Omega \boldsymbol{u}^F\, dV = \mathbf{0}$ and $\int_\Omega \boldsymbol{\nabla}\boldsymbol{u}^F\, dV = \int_{\partial\Omega} \boldsymbol{u}^F \otimes \boldsymbol{n}\, dS = \mathbf{0}$, cf. De Souza Neto et al. [19]. We satisfy the latter condition by enforcing periodic boundary conditions on $\boldsymbol{u}^F$, i.e. $\boldsymbol{u}^F(\boldsymbol{X}) = \boldsymbol{u}^F(\boldsymbol{X} - \boldsymbol{A}_j)$ for $\boldsymbol{X} \in \partial\Omega^{j+}$ and previously introduced lattice vectors $\boldsymbol{A}_j$, $j = 1, 2$. The periodic boundary conditions are enforced via

[2] $\delta(\,\cdot\,)$ denotes the variational operator.

Lagrange multipliers $\boldsymbol{\Lambda} : \partial\Omega^+ \to \mathbb{R}^2$ (Zhang and Khandelwal [59] and Bluhm et al. [8]), whereby the Hill-Mandel condition is expressed as

$$\begin{aligned}
&|\Omega|\delta\boldsymbol{F}^M\left(\boldsymbol{X}^M\right) : \boldsymbol{P}^M\left(\boldsymbol{X}^M\right) = \int_\Omega \delta\boldsymbol{F}(\boldsymbol{X}) : \boldsymbol{P}(\boldsymbol{X})\, dV \\
&-\sum_{j=1}^{2}\int_{\partial\Omega^{j+}} \boldsymbol{\Lambda}(\boldsymbol{X}) \cdot \left(\delta\boldsymbol{u}(\boldsymbol{X}) - \delta\boldsymbol{u}(\boldsymbol{X}-\boldsymbol{A}_j) - \delta\boldsymbol{F}^M\left(\boldsymbol{X}^M\right)\boldsymbol{A}_j\right)\, dS \\
&-\sum_{j=1}^{2}\int_{\partial\Omega^{j+}} \delta\boldsymbol{\Lambda}(\boldsymbol{X}) \cdot \left(\boldsymbol{u}(\boldsymbol{X}) - \boldsymbol{u}(\boldsymbol{X}-\boldsymbol{A}_j) - \left(\boldsymbol{F}^M\left(\boldsymbol{X}^M\right) - \boldsymbol{1}\right)\boldsymbol{A}_j\right)\, dS.
\end{aligned} \tag{4}$$

We require (4) to hold for any admissible $\delta\boldsymbol{F}^M$, $\delta\boldsymbol{\Lambda}$ and $\delta\boldsymbol{u}$. First, we equate $\delta\boldsymbol{F}^M = \boldsymbol{0}$ and evaluate the admissible $\boldsymbol{u}$ and $\boldsymbol{\Lambda}$ such that

$$\begin{aligned}
0 &= \int_\Omega \delta\boldsymbol{F}(\boldsymbol{X}) : \boldsymbol{P}(\boldsymbol{X})\, dV \\
&-\sum_{j=1}^{2}\int_{\partial\Omega^{j+}} \boldsymbol{\Lambda}(\boldsymbol{X}) \cdot \left(\delta\boldsymbol{u}(\boldsymbol{X}) - \delta\boldsymbol{u}(\boldsymbol{X}-\boldsymbol{A}_j) - \delta\boldsymbol{F}^M\left(\boldsymbol{X}^M\right)\boldsymbol{A}_j\right)\, dS \\
&-\sum_{j=1}^{2}\int_{\partial\Omega^{j+}} \delta\boldsymbol{\Lambda}(\boldsymbol{X}) \cdot \left(\boldsymbol{u}(\boldsymbol{X}) - \boldsymbol{u}(\boldsymbol{X}-\boldsymbol{A}_j) - \left(\boldsymbol{F}^M\left(\boldsymbol{X}^M\right) - \boldsymbol{1}\right)\boldsymbol{A}_j\right)\, dS.
\end{aligned} \tag{5}$$

for all admissible $\delta\boldsymbol{u}$ and $\delta\boldsymbol{\Lambda}$. Having $\boldsymbol{u}$ and $\boldsymbol{\Lambda}$, we next equate $\delta\boldsymbol{u} = \delta\boldsymbol{F}^M\boldsymbol{X}$ and $\delta\boldsymbol{\Lambda} = \boldsymbol{0}$ and use the arbitrariness of $\delta\boldsymbol{F}^M$ to reduce (4) to the stress homogenization relation

$$\boldsymbol{P}^M(\boldsymbol{X}^M) = \frac{1}{|\Omega|}\int_\Omega \boldsymbol{P}(\boldsymbol{X})\, dV. \tag{6}$$

If we instead equate $\delta\boldsymbol{F}^M = \boldsymbol{0}$, $\delta\boldsymbol{\Lambda} = \boldsymbol{0}$ and $\delta\boldsymbol{u}(\boldsymbol{X}) = \boldsymbol{B}\boldsymbol{X}$ for the arbitrary constant second order tensor $\boldsymbol{B}$, (4) reduces to

$$\int_\Omega \boldsymbol{P}(\boldsymbol{X})\, dV = \sum_{j=1}^{2}\int_{\partial\Omega^{j+}} \boldsymbol{\Lambda}(\boldsymbol{X}) \otimes \boldsymbol{A}_j\, dS, \tag{7}$$

using the arbitrariness of $\boldsymbol{B}$. Upon combining (7) and (6), we find that the homogenized stress is also computed as

$$\boldsymbol{P}^M(\boldsymbol{X}^M) = \frac{1}{|\Omega|}\sum_{j=1}^{2}\int_{\partial\Omega^{j+}} \boldsymbol{\Lambda}(\boldsymbol{X}) \otimes \boldsymbol{A}_j\, dS. \tag{8}$$

After obtaining the macroscopic first Piola-Kirchhoff stress from (8), the macroscopic Cauchy stress is computed as $\boldsymbol{\sigma}^M = \frac{1}{J^M}\boldsymbol{P}^M\left(\boldsymbol{F}^M\right)^T$.

To obtain the macroscopic response on our unit cell, we prescribe the macroscopic deformation gradient and compute the macroscopic Cauchy stress. For example, to mimic uniaxial

loading, we prescribe

$$\boldsymbol{\nabla}^M \boldsymbol{u}^M = \begin{bmatrix} \lambda & \nabla^M u^M_{12} \\ \nabla^M u^M_{21} & \nabla^M u^M_{22} \end{bmatrix}, \quad \text{such that} \quad \boldsymbol{P}^M = \begin{bmatrix} P^M_{11} & 0 \\ 0 & 0 \end{bmatrix}, \tag{9}$$

where λ is the load increment. We assume the macroscopic response is at least orthotropic, so that $\nabla^M u^M_{12} = 0$ and $\nabla^M u^M_{21} = 0$, cf. Wallin and Tortorelli [51]. Ultimately, we solve for $\boldsymbol{u}$ and $\boldsymbol{\Lambda}$ to satisfy (5), and $\nabla^M u^M_{22}$ to satisfy $P^M_{22} = 0$[3].

3. Topology optimization

Our unit cell constituent material is modeled by the hyperelastic isotropic compressible neo-Hookean strain energy

$$W = \frac{1}{4} K_o \left(\left(J^2 - 1 \right) - \ln \left(J^2 \right) \right) + \frac{1}{2} G_o \left(J^{-2/3} \mathrm{tr} \left(\boldsymbol{F}^T \boldsymbol{F} \right) - 3 \right), \tag{10}$$

where K_o and G_o are the bulk and shear modulii of the isotropic microscopic material in the limit of infinitesimal strain. The goal of our topology optimization is to distribute the material in the unit cell, Ω, to achieve the desired homogenized response. To quantify the material distribution, we use the continuous non-dimensional volume fraction field $z : \Omega \to [0, 1]$. We also consider square 2D unit cells that exhibit cubic symmetry as shown in Fig. 2, so we restrict the design space to the symmetry sector $\Omega^r \subset \Omega$, i.e. $z : \Omega^r \to [0, 1]$, whereby

$$z(\boldsymbol{Q}\boldsymbol{X}) = z(\boldsymbol{X}), \quad \text{for} \quad \boldsymbol{X} \in \Omega^r, \tag{11}$$

for each symmetry transformation $\boldsymbol{Q}$.

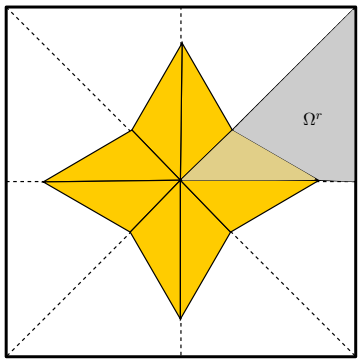

Fig. 2. Illustration of a square unit cell Ω with symmetry sector Ω^r.

A well-posed topology optimization problem is obtained using restriction, which we perform herein via the Helmholtz PDE-filter, cf. Lazarov and Sigmund [31]. In this way, z is replaced by the smooth periodic field $\nu : \Omega \to [0, 1]$, obtained by imposing stationarity on the

[3]Note that we require $P^M_{22} = 0$, i.e. we use the first Piola-Kirchhoff stress rather than the Cauchy stress. However, since $F^M_{12} = F^M_{21} = 0$ the $P^M_{22} = 0$ condition is equivalent to $\sigma^M_{22} = 0$.

potential

$$\begin{aligned}\Pi(\nu,\mu) = \quad & \frac{1}{2}\int_\Omega (\nu(\boldsymbol{X}) - z(\boldsymbol{X}))^2\, dV + \frac{1}{2}l^2 \int_\Omega |\boldsymbol{\nabla}\nu(\boldsymbol{X})|^2\, dV \\ & + \sum_{j=1}^{2} \int_{\partial\Omega^{j+}} \mu(\boldsymbol{X})(\nu(\boldsymbol{X}) - \nu(\boldsymbol{X} - \boldsymbol{A}_j))\, dS,\end{aligned} \tag{12}$$

where $\mu : \Omega \to \mathbb{R}$ is the Lagrange multiplier used to enforce the periodic boundary conditions on $\nu \in H^1$. By minimizing Π, we obtain a periodic ν that is "close" to z but smoother. The smoothness results from approximately enforcing the $|\boldsymbol{\nabla}\nu|^2 = 0$ constraint in Ω via the penalty method. Larger penalty parameters l^2 better approximate this constraint and hence lead to smoother ν fields. The stationarity of (12) leads to a constrained elliptical PDE that is similar to the elasticity problem (5); it is solved using standard finite elements, cf. the Appendix for details.

Unsurprisingly, the introduction of the filter results in regions wherein $\nu(\boldsymbol{X}) \in (0, 1)$. To limit the extent of these regions, we use thresholding (Guest et al. [23], Wang et al. [53]) and RAMP penalization (Stolpe and Svanberg [41]), such that the material parameters G_o and K_o in (10) are replaced by the interpolated counterparts

$$\begin{aligned} & G = \chi(\bar{\nu})G_o, \quad K = \chi(\bar{\nu})K_o, \\ & \text{where} \quad \chi(\bar{\nu}) = \frac{(1-\delta_o)\bar{\nu}}{1 + q(1-\bar{\nu})} + \delta_o, \\ & \text{and} \quad \bar{\nu} = H_{\beta,\eta}(\nu) = \frac{\tanh(\beta\eta) + \tanh(\beta(\nu-\eta))}{\tanh(\beta\eta) + \tanh(\beta(1-\eta))}. \end{aligned} \tag{13}$$

In (13), $\delta_o > 0$ is the ersatz void "material" stiffness scaling, and β and $\eta = 0.5$ are numerical parameters defined such that $\lim_{\beta\to\infty} H_{\beta,\eta}(\nu) = u_s(\nu - \eta)$, where u_s is the unit step function. Increasing values of $q > 0$ lead to increasing RAMP penalization.

3.1. Third medium contact method

In the contact model, we approximate contact pressure via the reactive tractions of an ersatz material, i.e. the third medium, that is placed between the contacting surfaces. Notably, this material already exists in the topology optimization; it is the void "material" in regions where $\bar{\nu} \approx 0$. As the third medium is compressed, $J \to 0$ and hence $W \to \infty$, which results in the reactive tractions. Unfortunately, this behavior also hinders the convergence of the finite element analysis because the elements in the third medium become highly distorted. To mitigate convergence issues, Bog et al. [9] decreased the polynomial order of the elements in the third medium. Alternatively, Bluhm et al. [7] augment the strain energy function to penalize bending and warping in the third medium, such that

$$W \leftarrow W + \mathcal{I}(\bar{\nu})W^H, \tag{14}$$

where

$$W^H = \frac{1}{2}k_r \mathbb{H}(\boldsymbol{u}) : \mathbb{H}(\boldsymbol{u}), \tag{15}$$

$\mathbb{H}(\boldsymbol{u})$ is the Hessian of the displacement field, $k_r = 1 \cdot 10^{-6} a^2 K_o$ is the penalization constant assigned by Bluhm et al. [7], and

$$\mathcal{I}(\bar{\nu}) = 1 - H_{\hat{\beta},\hat{\eta}}(\bar{\nu}), \tag{16}$$

is the void indicator function, where $\hat{\beta} = 500$ and $\hat{\eta} = 0.01$ replace β and η in (13). This indicator function is similar to that proposed by Wang et al. [53] in their energy interpolation regularization. We emphasize that (15) is introduced to limit excessive distortions in void regions, i.e. the augmented energy is solely a numerical convenience; it does not affect the response of the constituent material in the solid regions, were $\mathcal{I}(\bar{\nu}) \approx 0$.

Bluhm et al. [7] introduce an ad hoc scaling $P(J) = e^{-5J}$ to the first variation of (15), such that $P(J) \to 1$ as $J \to 0$ and $P(J) \to 0$ as $J \to \infty$. Since δW is scaled by $P(J)$, but not W^H, no potential exists which leads to an unsymmetric stiffness matrix, and necessitates the use of special linear solvers with increased memory requirements. Based on our numerical investigations, we found that removing this scaling had minimal impact on both the results and numerical stability, so we do not use it.

3.2. Topology optimization problem

We use topology optimization to tailor the homogenized macroscopic stress-strain behavior, such that the uniaxial Cauchy stress, σ_{11}^M, matches the prescribed target, $\bar{\sigma}^M$. This is accomplished by minimizing the cost function

$$g_o = \sum_{j=1}^{N_p} g_o^j = \sum_{j=1}^{N_p} w^j \left| \sigma_{11}^{M,j} - \bar{\sigma}^{M,j} \right|^2, \tag{17}$$

where $w^j > 0$ are the weights and $j = \{1, 2, ..., N_p\}$ are the λ_j load steps at which the Cauchy stress $\boldsymbol{\sigma}^{M,j}$ is computed. The topology optimization problem thereby reads

$$(\mathbb{TO}) \quad \begin{cases} \min\limits_{z \in [0,1]} \quad g_o. \end{cases} \tag{18}$$

We use the gradient based non-linear programming method MMA (Svanberg [43]) to solve (18), wherefore the gradients of the cost function, g_o, with respect to the design variables, z, are required. The sensitivity analysis is performed via the adjoint method, cf. the Appendix for details.

4. Shape optimization

Without the use of adaptive mesh refinement or remeshing strategies, the topology optimized designs invariably have poorly resolved boundaries. As a result, the contact conditions are not precisely modeled. To mitigate these effects, we follow the topology optimization with a shape optimization to more accurately model the deformation in the unit cell. That said, to simplify the contact modeling, we again use the third medium formulation.

In our shape optimization, a design deformation $\boldsymbol{\varphi}_d$ deforms the initial design configuration Ω_o (interpretation from the topology optimized design) into the shape optimized design configuration $\Omega = \boldsymbol{\varphi}_d(\Omega_o)$, such that $\boldsymbol{\varphi}_d(\boldsymbol{X}_o) = \boldsymbol{X}_o + \boldsymbol{d}(\boldsymbol{X}_o)$, where $\boldsymbol{d} : \Omega_o \to \mathbb{R}^2$ is the design

displacement field, cf. Fig. 3. The use of a shape optimization design field is similar to the use of a volume fraction design field in the topology optimization.

To formulate a well-posed shape optimization problem, we use a PDE filter, again mimicking topology optimization. The PDE filter is similar to the *fictitious energy approach*, developed by Scherer et al. [36], and recently revisited by Swartz et al. [44]. In our PDE filter, $\boldsymbol{d}$ is used to obtain the smoothed design displacement $\boldsymbol{\psi}$ resulting from the application of a Robin boundary condition involving $\boldsymbol{d}$ to $\partial\Omega_o^d$, where $\partial\Omega_o^d$ is the shape optimized boundaries, which means that we have a reduced design space $\boldsymbol{d} : \partial\Omega_o^d \to \mathbb{R}^2$, defined solely on the boundary $\partial\Omega_o^d$. This defines the smoothed domain $\Omega = \boldsymbol{\varphi}_\psi(\Omega_o)$ such that $\boldsymbol{X} = \boldsymbol{\varphi}_\psi(\boldsymbol{X}_o) = \boldsymbol{X}_o + \boldsymbol{\psi}(\boldsymbol{X}_o)$. We evaluate the optimization cost and constraint functions over this smoothed domain Ω, i.e. it ultimately provides the optimized design.

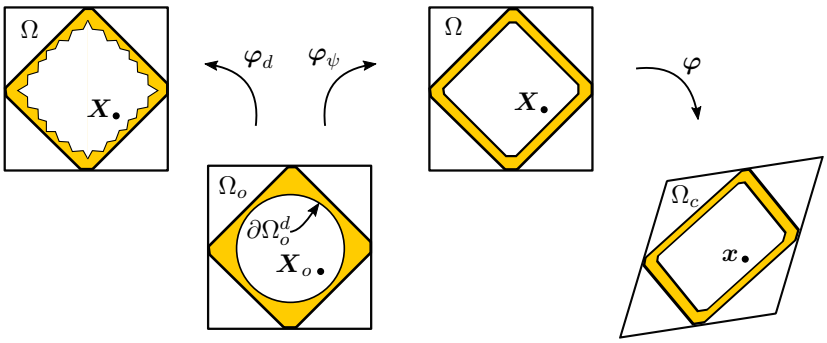

Fig. 3. The mappings $\boldsymbol{\varphi}_d$, $\boldsymbol{\varphi}_\psi$ and $\boldsymbol{\varphi}$.

More precisely, we obtain $\boldsymbol{\psi}$ by invoking stationarity on the potential

$$\begin{aligned}\Gamma(\boldsymbol{\psi}, \boldsymbol{\Upsilon}) = \quad & \int_{\Omega_o} W_\psi \, dV + \frac{1}{2}\int_{\partial\Omega_o^d} ||\boldsymbol{\psi}(\boldsymbol{X}_o) - \lambda_d \boldsymbol{d}(\boldsymbol{X}_o)||^2 \, dS \\ & + \sum_{j=1}^{2} \int_{\partial\Omega_o^{j+}} \boldsymbol{\Upsilon}(\boldsymbol{X}_o) \cdot (\boldsymbol{\psi}(\boldsymbol{X}_o) - \boldsymbol{\psi}(\boldsymbol{X}_o - \boldsymbol{A}_j)) \, dS\end{aligned} \tag{19}$$

where W_ψ is the neo-Hookean filter energy and $\boldsymbol{\Upsilon} : \partial\Omega_o^+ \to \mathbb{R}^2$ is the Lagrange multiplier which enforces periodicity[4]. In the above, $\lambda_d \in [0, 1]$ is a numerical scaling parameter, analogous to λ in (9), which we increment until $\lambda_d = 1$. To ensure that our unit cell remains square, we define the admissible $\boldsymbol{\psi} \in \mathcal{V} = \{\boldsymbol{\psi} \in H^1 : \boldsymbol{\psi}(\boldsymbol{X}_o) \cdot \boldsymbol{e}_2 = \boldsymbol{0}$ for $\boldsymbol{X}_o \in \partial\Omega^{1-}$, $\boldsymbol{\psi}(\boldsymbol{X}_o) \cdot \boldsymbol{e}_1 = \boldsymbol{0}$ for $\boldsymbol{X}_o \in \partial\Omega^{2-}\}$. The parameters in W_ψ, are defined as $K_\psi = G_\psi = 1$ mm in solid regions, and $K_\psi = G_\psi = \delta_o$ mm in void regions. The stationarity of (19) is solved using standard finite elements, cf. the Appendix for details.

We design 2D unit cells with cubic symmetry, by restricting the design space to the internal boundaries, $\partial\Omega_o^r \subset \partial\Omega_o^d$, of the symmetry sector Ω_o^r, analogously to our assignment of the volume fraction field over the symmetry sector in the topology optimization. This design

[4]The $(\,\cdot\,)_\psi$ notation is used to indicate variables associated with $\boldsymbol{\psi}$.

displacement is defined over the entirety of the unit cell via the symmetry transformation

$$\boldsymbol{d}(\boldsymbol{Q}\boldsymbol{X}) = \boldsymbol{d}(\boldsymbol{X}). \tag{20}$$

4.1. Shape optimization problem

We use the same objective function for the shape optimization problem as for the topology optimization, i.e. to tailor the homogenized macroscopic stress-strain behavior, such that the uniaxial Cauchy stress, σ_{11}^M, matches the prescribed target stress, $\bar{\sigma}^M$, cf. (17). The shape optimization problem we solve is stated as

$$(\mathbb{SO}) \quad \begin{cases} \min\limits_{\boldsymbol{d}\in\mathcal{B}} \ g_o, \end{cases} \tag{21}$$

where $\mathcal{B}$ is the set of H^1 functions subjected to box constraints.

5. Numerical examples

Our design domain is a square unit cell with side-length $a = 10$ mm. The size of the unit cell is a user input, and can be chosen as deemed fit. The assumption of length-scale separation must however hold. The reduction to two-dimensions is obtained by assuming plane strain deformation. The constituent solid material has Young's modulus $E = 700$ MPa and Poisson's ratio $\nu = 0.34$, which provides $K_o = E/3(1-2\nu)$ and $G_o = E/2(1+\nu)$ in (10). Our framework can accommodate multiple components of the macroscopic stress tensor. However, herein we limit ourselves to a single component, namely σ_{11}^M. We emphasize that we are able to obtain "crisp" topology optimized designs without an active volume constraint.

5.1. Topology optimization

We discretize our state and filter equations using an 80×80 mesh. The ersatz material stiffness is $\delta_o = 10^{-4}$, the RAMP penalization is $q = 8$ and the filter length scale[5] $l = 0.5/(2\sqrt{3}) \approx 0.144$ mm, cf. (12). This relatively high δ_o value was necessary to ensure that the finite element analyses converged. The Heaviside projection (13) is enabled after 200 design iterations with $\beta = 1$ and and subsequently updated $\beta \leftarrow 2\beta$ every 50th iteration until $\beta = 128$. We solve (4) using the modified generalized displacement control method (MGDCM) (Leon et al. [33]) in a total Lagrangian framework, wherein the displacement field is approximated using standard quadratic serendipity finite elements, whereas the filtered volume fraction field is approximated using linear quadrilateral elements, cf. the Appendix for details. We solve our optimization problem using the MMA-scheme, cf. Svanberg [43]. To reduce the likelihood of obtaining disconnected structures, the unit cell is loaded both in compression and tension, cf. Swartz et al. [45].

The initial density distribution for the first example is $z = 0.7$ everywhere except over the centrally located circular hole of radius 1.5 mm, where $z = 10^{-4}$. We emphasize that topology optimization can be sensitive to changes in the initial design and the algorithmic parameters. The optimization targets and weights for the first example are denoted in Tab. I, cf. (17), and the optimized design is illustrated in 4. We chose these target values to illustrate the

[5]This corresponds to four element lengths, i.e. 0.5 mm, in a traditional convolution filter, cf. Lazarov and Sigmund [31].

benefits of contact, but emphasize that their assignment is user dependent. The inclusion of the arbitrarily chosen 10% tensile stretch ensures the structures can support tensile loads. The choice of weights was mainly based on experience gained during the numerical analyses.

Tab. I. The optimization targets and weights corresponding to the Fig. 4 design.

Target stretch	0.95	0.90	0.85	0.80	0.75	0.60	1.1
Target σ_{11}^M	-1.0	-3.0	-5.0	-7.0	-9.0	-80	10
Weights w	10	10	100	100	100	10	100

As seen in the figure, the homogenized response approaches the target response. The sudden decrease in uniaxial macroscopic stress for stretches below 0.7 is attributed to the internal contact, cf. Fig. 5. The full evolution of the von Mises stress response can be seen in the movie provided as supplementary material, cf. Appendix B.

We emphasize that the inherent non-linearity of the contact problem leads to convergence issues in the analysis if the step length $\Delta\lambda$ is too large. We mitigate these issues by employing a restart scheme in our MGDCM implementation, such that, if inverted elements or loss of convergence is encountered, the analysis is restarted with a smaller load step. Alternatively, a line-search procedure could be implemented, cf. Bog et al. [9].

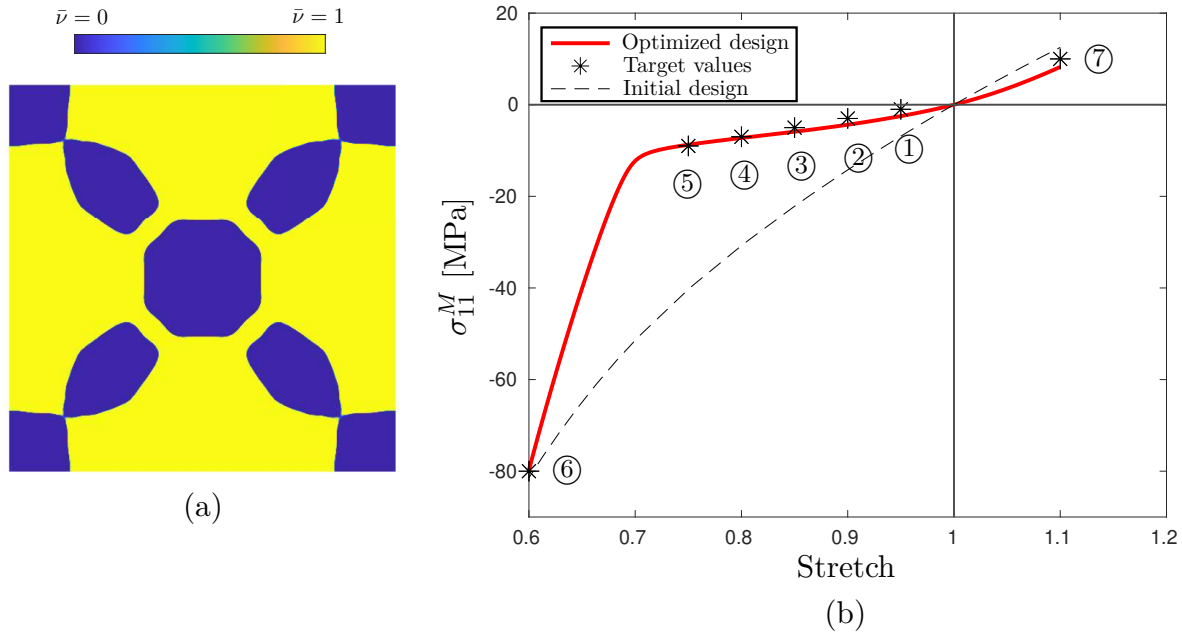

Fig. 4. The undeformed unit cell design obtained when using the targets and weights in Tab. I (a) and corresponding macroscopic uniaxial stress versus stretch (b).

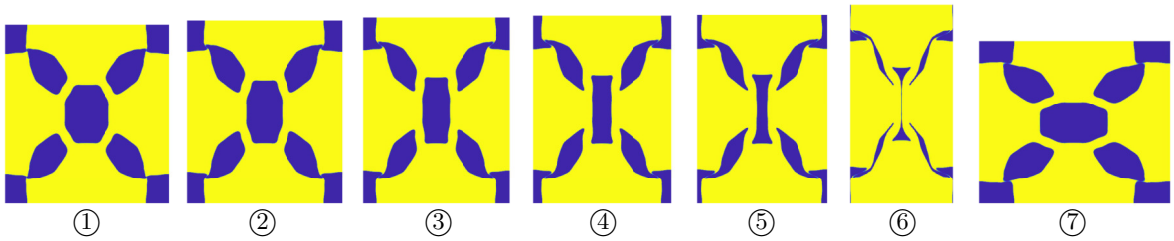

Fig. 5. Snapshots of the Fig. 4(a) design's deformed configurations at the target stretches.

In the second example, the initial density distribution is $z = 0.7$ everywhere except over nine equally spaced circular holes (with center-point coordinates $(x, y) \in \{(2, 2), (2, 5), (2, 8), (5, 2), ...\}$ and radii 1.5 mm), where $z = 10^{-4}$. The targets and weights of Tab. II are employed. We also include a volume constraint in the optimization formulation, such that the volume of the structure should not exceed 45% of the total volume of the unit cell. This volume constraint is however inactive in the final design. The resulting design is depicted in Fig. 6.

Tab. II. The optimization targets and weights corresponding to the Fig. 6 design.

Target stretch	0.95	0.90	0.85	0.80	0.75	0.60	1.1
Target σ_{11}^M	-5.0	-5.0	-5.0	-5.0	-5.0	-40	10
Weights w	1.0	1.0	100	100	100	10	100

We see that the design leverages the internal contact without full compaction to achieve the desired response, cf. Fig. 7. To further strengthen this claim, we plot the von Mises stress at the target stretches in Fig. 8, where it is seen that the stress field is not homogeneous, therefore full compaction does not occur. The full evolution of the von Mises stress response can be seen in the movie provided as supplementary material, cf. Appendix B.

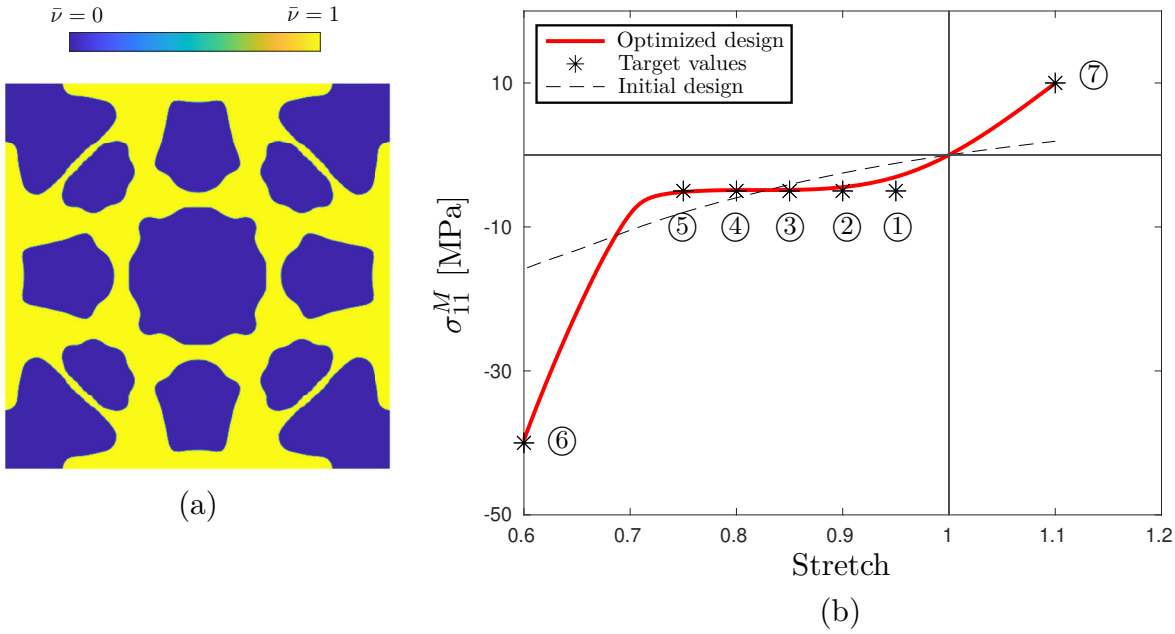

Fig. 6. The undeformed unit cell design obtained when using the targets and weights in Tab. II (a) and corresponding macroscopic uniaxial stress versus stretch (b)

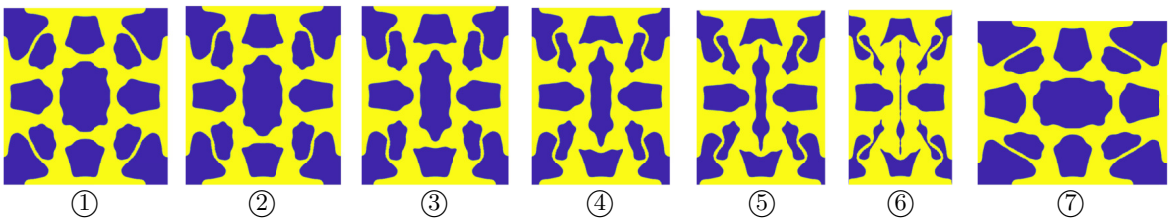

Fig. 7. Snapshots of the Fig. 6(a) design's deformed configurations at the target stretches.

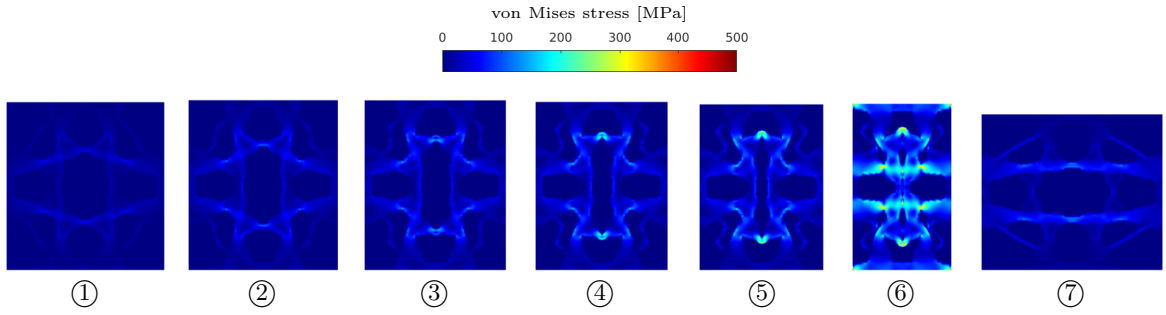

Fig. 8. Snapshots of the Fig. 6(a) design's von Mises stress distributions at the target stretches.

In the third example, the initial density distribution is $z = 0.4$ everywhere except over the centrally located circular hole of radius 1.5 mm, where $z = 10^{-4}$, and the targets and weights

of Tab. III are employed. The resulting design is depicted in Fig. 9.

Tab. III. The optimization targets and weights corresponding to the Fig. 9 design.

Target stretch	0.95	0.90	0.85	0.80	0.75	0.60	1.1
Target σ_{11}^M	-2.0	-4.0	-5.0	-5.0	-5.0	-40	10
Weights w	1.0	1.0	100	100	100	10	100

Fig. 10 depicts the snapshots of the Fig. 9(a) design's deformed configurations at the target stretches.

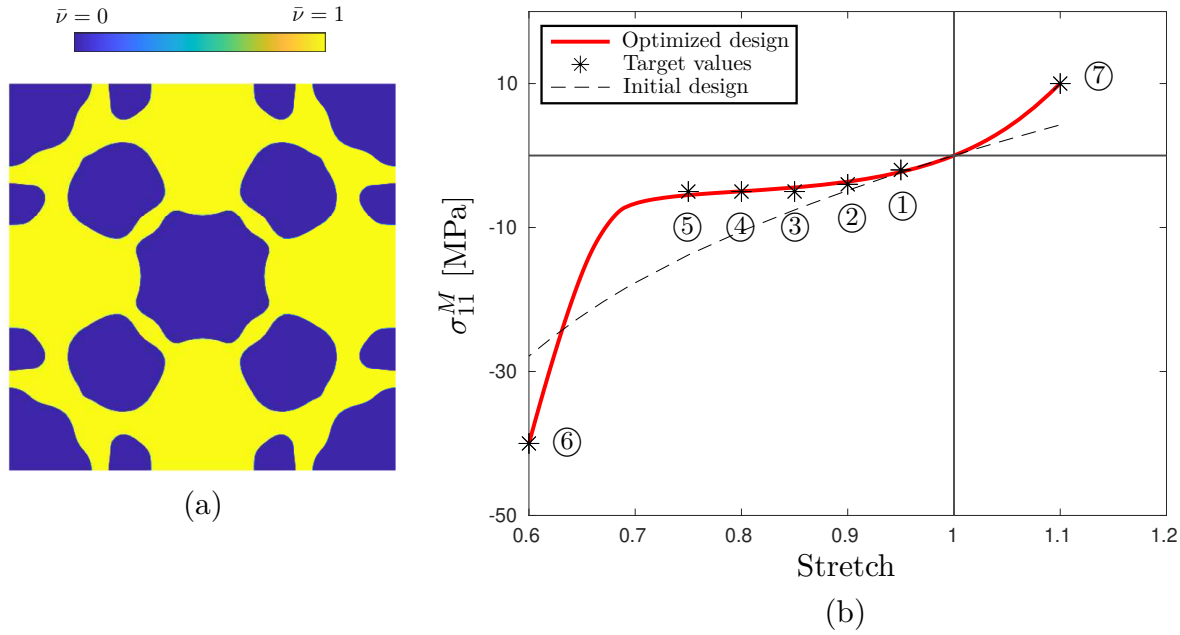

Fig. 9. The undeformed unit cell design obtained when using the targets and weights in Tab. II (a) and corresponding macroscopic uniaxial stress versus stretch (b).

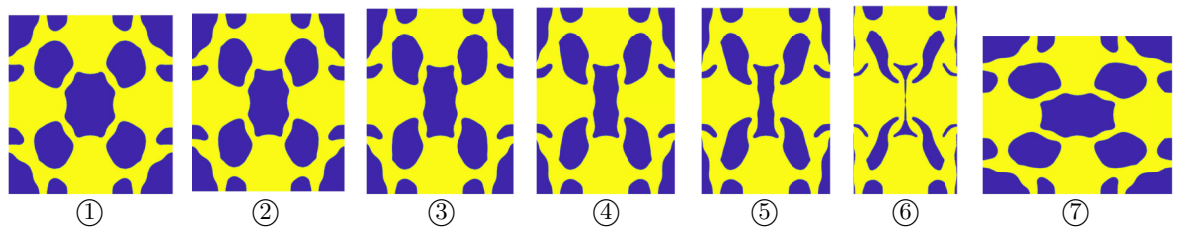

Fig. 10. Snapshots of the Fig. 9(a) design's deformed configurations at the target stretches.

5.2. Shape optimization

The Figs. 4-9 designs obtained by the density-based topology optimization have poorly resolved boundaries due to the use of the ersatz material and the coarse finite element mesh, cf. Fig. 11. To mitigate this effect, the Xtended finite element method (Villanueva and

Maute [48]) could be used in combination with the topology optimization. Here, we instead use shape optimization to further improve the topology optimized Fig. 9 design. The $\bar{\nu} = 0.5$ contour of the topology optimized design defines the boundary of the initial design that is shape optimized[6]. To model the contact in the shape optimization, we again use the third medium contact approach, wherefore we discretize the entire unit cell, i.e. we model the void-third medium phase via a conforming mesh. The mesh consists of 13832 fully integrated 2D quadratic triangular elements. The design displacement degrees-of-freedom are bounded by the box constraints $\mathcal{B} = \{\boldsymbol{d} \in H^1 : \boldsymbol{d} \cdot \boldsymbol{e}_i \in [-0.3, 0.3] \text{ mm}\}$.

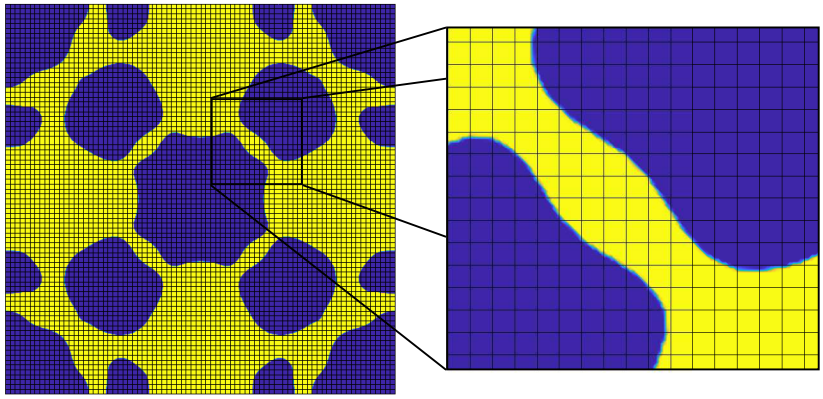

Fig. 11. The coarse 80×80 mesh used to obtain the Fig. 9 design.

Fig. 12(a) illustrates the shape optimized design obtained from the Fig. 9(a) topology optimized design. In Fig. 14, we show a zoom-in of the Fig. 12(b) stress versus stretch plot, to illustrate how the shape optimization improves the topology optimized design, i.e. initial design for the shape optimization. Fig. 15 depicts the difference between the initial and shape optimized designs. Clearly, small shape alternations impact the response. Fig. 13 depicts snapshots of the deformed configurations of the Fig. 12(a) design for the target stretches.

[6]See the Appendix for post-processing of the topology optimized design when using various level-sets $\bar{\nu} = C$, $C \in [0, 1]$.

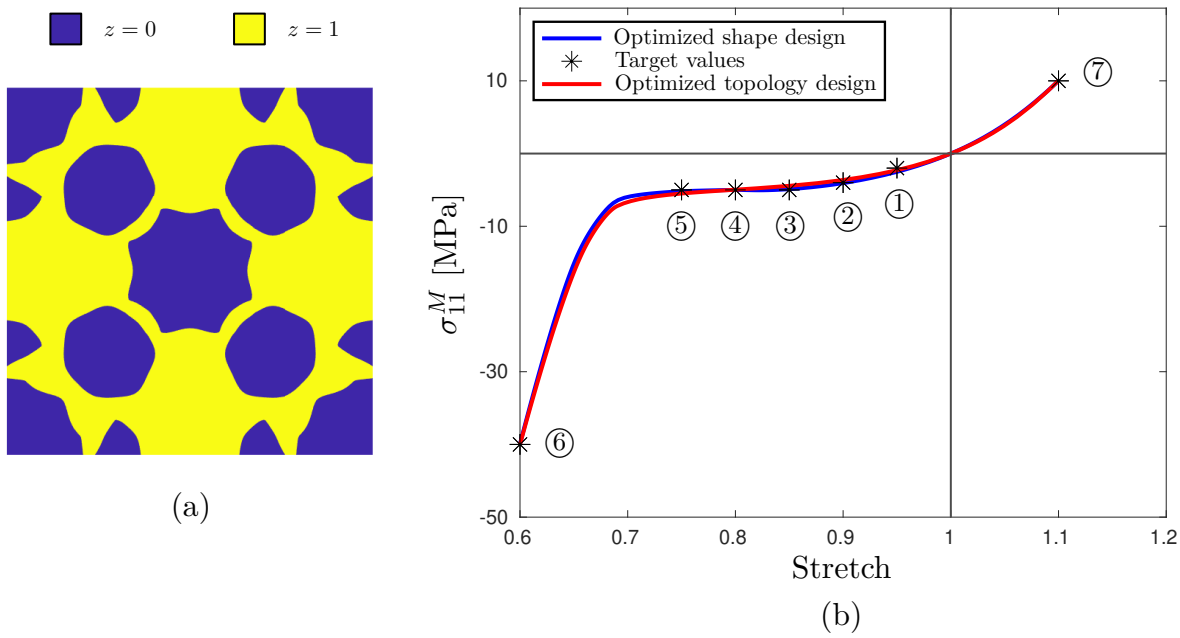

Fig. 12. The undeformed unit cell design obtained from a shape optimization of the Fig. 9(a) topology optimized design using the targets and weights in Tab. II (a), corresponding macroscopic uniaxial stress versus stretch (b) and deformed unit cell design at maximum compression (c).

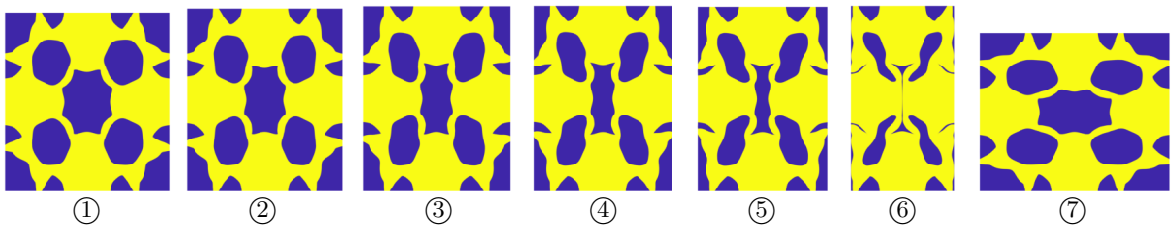

Fig. 13. Snapshots of the Fig. 12(a) design's deformation patterns at target stretches.

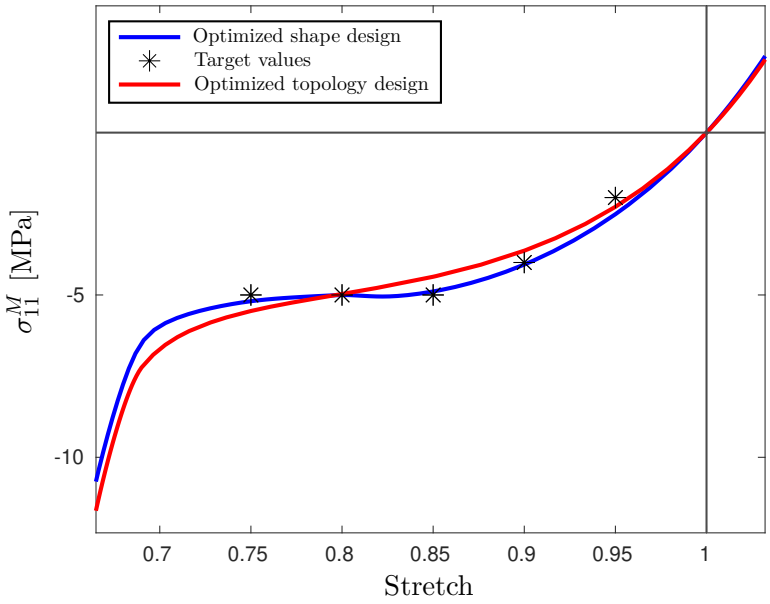

Fig. 14. A zoom-in on the macroscopic uniaxial stress versus stretch plot depicted in Fig. 12.

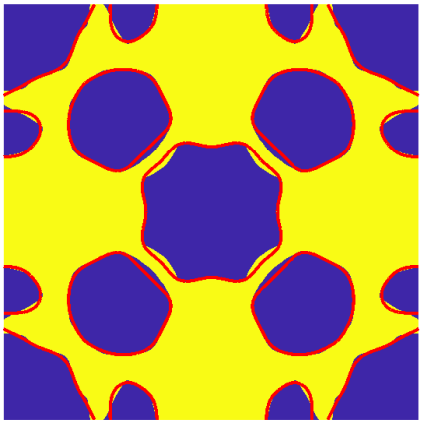

Fig. 15. The shape optimization alternations to the Fig. 9(a) unit cell design. The red boundary illustrates the initial design.

We emphasize that we encountered convergence issues when performing the shape optimization, which we attribute to the low stiffness elements in the third medium.

5.3. Post-processing

As a last step in our workflow, we conduct a post-processing analysis of the Fig. 12(a) shape optimized design in ABAQUS/EXPLICIT with a standard penalty contact formulation. The hyperelastic material (10) is implemented in a VUMAT user subroutine. We load the structure quasi-statically such that dynamic effects are negligible and we enforce the periodic boundary conditions using multipoint constraints following the virtual node method, cf. Danielsson et al. [18]. This analysis requires special care to model the internal contact

between opposing faces, as regions of the design interior might protrude into neighboring unit cells which is non-physical. To model this phenomenon, rigid frictionless contact surfaces are placed on the unit cell boundaries, cf. Fig. 16.

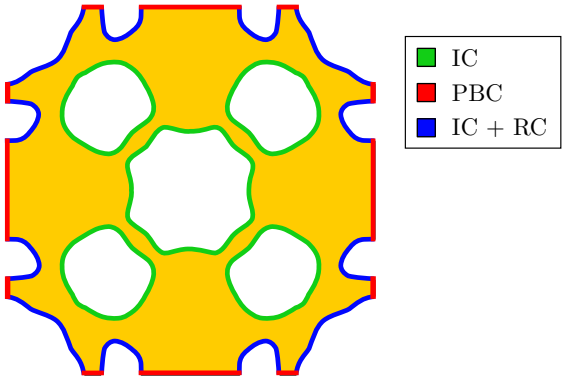

Fig. 16. Boundary conditions in ABAQUS simulation. Internal contact (IC) over green boundaries, periodic boundary conditions (PBC) over red boundaries and rigid contact (RC) + (IC) over blue boundaries.

The responses of the Fig. 9(a) topology and Fig. 12(a) shape optimized designs when modeling the contact using the third medium and penalty approaches, appear side-by-side in Fig. 17. Overall, we observe a good agreement between the contact models, but the onset of contact is slightly different. We also see that the response of the third medium formulation is in better agreement with that obtained by the penalty formulation for the shape optimized design than for the topology optimized design. These results also indicate that the relatively large ersatz stiffness δ_o does not significantly influence the response of our designs. The full evolution of the von Mises stress response can be seen in the movie provided as supplementary material, cf. Appendix B.

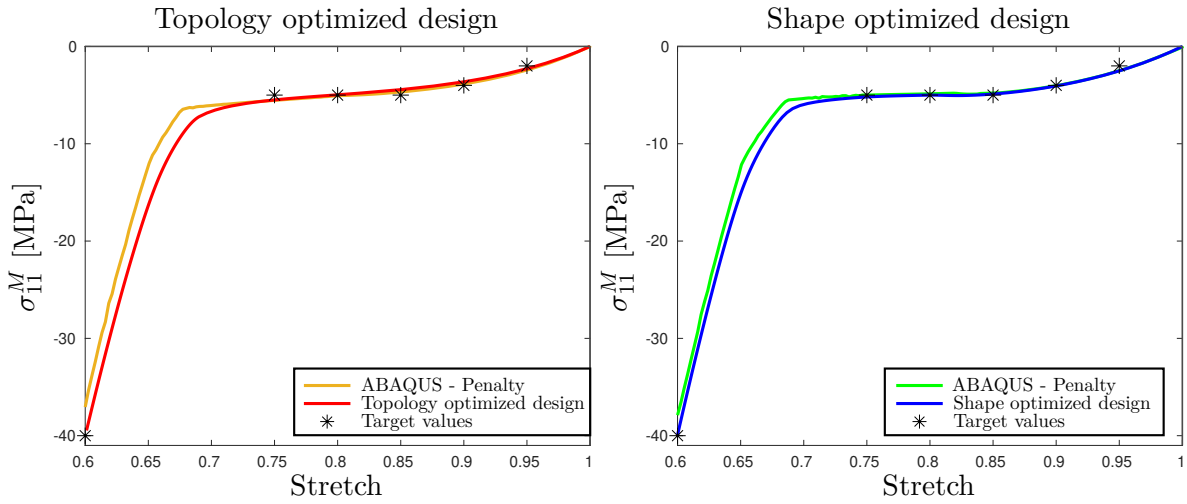

Fig. 17. The macroscopic uniaxial stress versus stretch for the topology and shape optimized designs using the third medium (red and blue) and penalty (orange and green) formulations.

6. Conclusions

In this work, we design metamaterials with prescribed macroscopic uniaxial stress versus stretch response using topology and shape optimization. A fully non-linear hyperelastic framework is employed with the third medium contact formulation. The topology optimized designs are post-processed using a nodal based shape optimization. The resulting shape optimized design outperforms its topology optimized counterpart, and exhibits a structural response that is in good agreement with that obtained by a standard penalty contact formulation.

Clearly, the third medium contact model in combination with topology optimization is a promising tool for generating designs which exhibit internal contact. However, our experience is that the method is very sensitive to perturbations in the design boundaries which are affected by the length-scale l of the filter (12), the steepness β in the Heaviside threshold (13) and the ersatz stiffness δ_o. Indeed, small changes in the aforementioned parameters could lead to the loss of convergence in the finite element analyzes, even with the restart and adaptive step length schemes. These numerical issues arise from inverted or excessively distorted elements in the third medium. Similar findings regarding convergence issues in the third medium approach are reported in Bog et al. [9] and Kruse et al. [28].

The shape optimization using the third medium also proved to be problematic. Notably, we were only able to make one design converge. This is attributed to the distinct boundary, i.e. sharp interface, in the conforming mesh design, which cause abrupt changes in the element stiffnesses which further degrades the convergence of the finite element simulations. Shape optimization via third medium certainly warrants further investigation.

Finally, we neglect the occurrence of structural instabilities in this work. Means for addressing buckling in the design of non-linear metamaterials exist, however they would greatly increase the computational complexity, cf. e.g. Zhang et al. [58]. This is also something to be addressed in future work.

Acknowledgments

This work was performed under the auspices of the U.S. Department of Energy by Lawrence Livermore Laboratory under Contract DE-AC52-07NA27344. The Swedish energy agency (grant nbr. 48344-1), the Swedish research council (grant nbr. 2021-03851) and eSSENCE: The e-Science Collaboration (grant nbr. 2020 6:1) are also gratefully acknowledged. The computations were enabled by resources provided by LUNARC. Last but not least, the authors would like to thank Prof. Ole Sigmund, Dr. Gore Lukas Bluhm and Dr. Konstantinos Poulios for helpful discussions during the research project.

Appendix A

Post-processing of a topology optimized design

The process of extracting the topology optimized design is non-unique, since the $\nu(\boldsymbol{X}) = C$ level set, at which we define the boundary, depends on the value of $C \in [0, 1]$. Obviously, different C values will yield different designs with different mechanical response. To illustrate this effect, we import the $C \in [0.48, 0.49, ..., 0.52]$ interpretations of the Fig. 9(a) design into ABAQUS/EXPLICIT and perform the simulations using conforming meshes of roughly 3600 CPE6M elements and a standard penalty contact formulation. The resulting macroscopic

uniaxial stress versus stretch curves appear in Fig. 18. Unsurprisingly, we observe that slight changes in C affect the mechanical response.

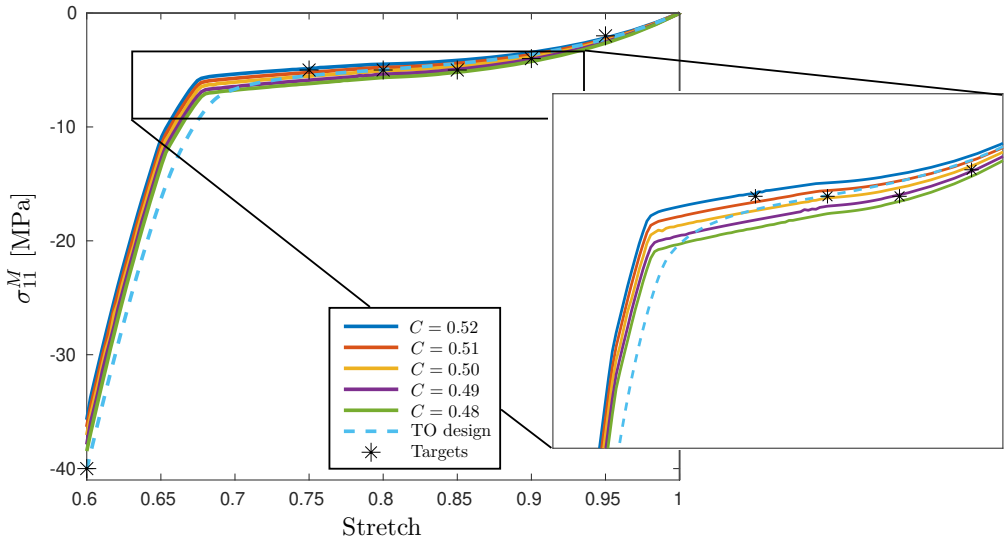

Fig. 18. Macroscopic uniaxial stress versus stretch when defining the Fig. 9(a) design using the level sets $C \in [0.48, 0.49, ..., 0.52]$.

Total Lagrangian FE-formulation

We discretize (4) using a structured finite element mesh over the square unit cell. A Galerkin based FE-formulation (cf. e.g. Crisfield [16]) is utilized, wherein both physical and variational displacement fields are approximated using quadratic element polynomial shape functions $\mathbf{N}$, e.g. $\boldsymbol{u}(\boldsymbol{X}, t) \approx \mathbf{N}(\boldsymbol{X})\mathbf{u}_e(t)$ and $\delta\boldsymbol{u}(\boldsymbol{X}) \approx \mathbf{N}(\boldsymbol{X})\delta\mathbf{u}_e$, where $\mathbf{u}_e(t)$ and $\delta\mathbf{u}_e$ are element nodal displacement and virtual displacement vectors. We enforce the periodicity constraints nodal-wise which requires the mesh to be symmetric with respect to the coordinate axes.

The FE-discretization of (4) when introducing the third medium penalization (14) becomes

$$\begin{aligned} &\delta\mathbf{u}^T \left(\mathbf{T}^T \boldsymbol{\Lambda} - \sum \left(\int_{\Omega^e} \boldsymbol{\nabla}\mathbf{N}^T \mathbf{P}\, dV + \int_{\Omega^e} k_r \mathcal{I} \mathbf{H}^T \mathbf{H}\mathbf{u}^e\, dV \right) \right) \\ &+\delta\mathbf{F}^{M,T} \left(|\Omega| \mathbf{P}^M - \mathbf{L}^T \boldsymbol{\Lambda} \right) \\ &+\delta\boldsymbol{\Lambda}^T \left(\mathbf{T}\mathbf{u} - \mathbf{L}\boldsymbol{\nabla}^M \boldsymbol{u}^M \right) = 0, \end{aligned} \tag{22}$$

where $\sum$ is the assembly operator, $\delta\mathbf{F}^M = \boldsymbol{\nabla}^M \delta\boldsymbol{u}^M$ and we introduce $\mathbf{L} \in \mathbb{R}^{2m \times 4}$ such that $\mathbf{L}\boldsymbol{\nabla}^M \boldsymbol{u}^M = (\boldsymbol{F}^M - \mathbf{1})\boldsymbol{A}_j$. In the above, the transformation matrix $\mathbf{T} \in \mathbb{R}^{2m \times n}$ is introduced such that $\mathbf{u}^+ - \mathbf{u}^- = \mathbf{T}\mathbf{u}$, where $\mathbf{u}^\pm \in \mathbb{R}^{2m}$ denotes nodal microscopic displacement on $\partial\Omega^\pm$ (cf. Zhang and Khandelwal [59]). We assume that there exist m pairs of mating boundary

nodes on $\partial\Omega$. In this way, $\mathbf{L}$ is constructed as

$$\mathbf{L} = \left[\mathbf{L}_{11}, \mathbf{L}_{21}, \mathbf{L}_{12}, \mathbf{L}_{22}\right] = \begin{bmatrix} \Delta X_1 & 0 & \Delta Y_1 & 0 \\ 0 & \Delta X_1 & 0 & \Delta Y_1 \\ \Delta X_2 & 0 & \Delta Y_2 & 0 \\ 0 & \Delta X_2 & 0 & \Delta Y_2 \\ \vdots & \vdots & \vdots & \vdots \\ \Delta X_m & 0 & \Delta Y_m & 0 \\ 0 & \Delta X_m & 0 & \Delta Y_m \end{bmatrix}, \tag{23}$$

where e.g. $\Delta X_1 = X_1^+ - X_1^-$.

In (22), $\mathbf{H}$ is the matrix which contains the second order derivatives of the shape functions $\mathbf{N}$ with respect to $\boldsymbol{X}$. In our isoparametric formulation, we have $\boldsymbol{\nabla}_\xi \mathbf{N} = \boldsymbol{J}\boldsymbol{\nabla}\mathbf{N}$, where $\boldsymbol{\nabla}_\xi$ is the gradient with respect to $\boldsymbol{\xi}$ and $\boldsymbol{J}$ is the Jacobian. By differentiating the above relation again with respect to $\boldsymbol{\xi}$ and rearranging, we find the linear system of equations which yields the sought second order derivatives, i.e.

$$\underbrace{\begin{bmatrix} \left(\frac{\partial X_1}{\partial \xi_1}\right)^2 & \left(\frac{\partial X_2}{\partial \xi_1}\right)^2 & 2\frac{\partial X_2}{\partial \xi_1}\frac{\partial X_1}{\partial \xi_1} \\ \left(\frac{\partial X_1}{\partial \xi_2}\right)^2 & \left(\frac{\partial X_2}{\partial \xi_2}\right)^2 & 2\frac{\partial X_2}{\partial \xi_2}\frac{\partial X_1}{\partial \xi_2} \\ \frac{\partial X_1}{\partial \xi_1}\frac{\partial X_1}{\partial \xi_2} & \frac{\partial X_2}{\partial \xi_1}\frac{\partial X_2}{\partial \xi_2} & \frac{\partial X_2}{\partial \xi_1}\frac{\partial X_1}{\partial \xi_2} + \frac{\partial X_1}{\partial \xi_1}\frac{\partial X_2}{\partial \xi_2} \end{bmatrix}}_{\boldsymbol{M}} \underbrace{\begin{bmatrix} \frac{\partial^2 \mathbf{N}}{\partial X_1^2} \\ \frac{\partial^2 \mathbf{N}}{\partial X_2^2} \\ \frac{\partial^2 \mathbf{N}}{\partial X_1 \partial X_2} \end{bmatrix}}_{\boldsymbol{y}} = \underbrace{\begin{bmatrix} \frac{\partial^2 \mathbf{N}}{\partial \xi_1^2} - \frac{\partial \mathbf{N}}{\partial X_1}\frac{\partial^2 X_1}{\partial \xi_1^2} - \frac{\partial \mathbf{N}}{\partial X_2}\frac{\partial^2 X_2}{\partial \xi_1^2} \\ \frac{\partial^2 \mathbf{N}}{\partial \xi_2^2} - \frac{\partial \mathbf{N}}{\partial X_1}\frac{\partial^2 X_1}{\partial \xi_2^2} - \frac{\partial \mathbf{N}}{\partial X_2}\frac{\partial^2 X_2}{\partial \xi_2^2} \\ \frac{\partial^2 \mathbf{N}}{\partial \xi_1 \partial \xi_2} - \frac{\partial \mathbf{N}}{\partial X_1}\frac{\partial^2 X_1}{\partial \xi_1 \partial \xi_2} - \frac{\partial \mathbf{N}}{\partial X_2}\frac{\partial^2 X_2}{\partial \xi_1 \partial \xi_2} \end{bmatrix}}_{\boldsymbol{b}}. \tag{24}$$

Now, we specialize (22) to uniaxial loading conditions. Using the arbitrariness of $\delta\mathbf{u}$, $\delta\boldsymbol{\Lambda}$ and $\delta\mathbf{F}^M$ in (22) yields the residual equations

$$\mathbf{r}^*(\mathbf{u}^*) = \begin{bmatrix} \mathbf{r_u} \\ \mathbf{r}_{\boldsymbol{\Lambda}} \\ \mathbf{r}_{\boldsymbol{F}} \end{bmatrix} = \mathbf{0}, \tag{25}$$

where $\mathbf{u}^* = [\mathbf{u}, \boldsymbol{\Lambda}, \nabla^M u_{22}^M]^T$, $\mathbf{r_u} = \sum \left(\int_{\Omega^e} \boldsymbol{\nabla}\mathbf{N}^T \mathbf{P}\, dV + \int_{\Omega^e} k_r \mathcal{I} \mathbf{H}^T \mathbf{H}\mathbf{u}^e\, dV \right) - \mathbf{T}^T\boldsymbol{\Lambda}$, $\mathbf{r}_{\boldsymbol{\Lambda}} = -\mathbf{T}\mathbf{u} + \mathbf{L}_{22}\nabla^M u_{22}^M + \lambda \mathbf{L}_{11}$ and $\mathbf{r}_{\boldsymbol{F}} = -|\Omega| P_{22}^M + \mathbf{L}_{22}^T \boldsymbol{\Lambda}$. The generalized displacement vector $\mathbf{u}^*$ which fulfills (25) is found from the linearization

$$\begin{aligned} &\mathbf{r}^*(\mathbf{u}^* + \delta\mathbf{u}^*, \lambda + d\lambda) \approx \mathbf{r}^* + \frac{\partial \mathbf{r}^*}{\partial \mathbf{u}^*} d\mathbf{u}^* + \frac{\partial \mathbf{r}^*}{\partial \lambda} d\lambda = \mathbf{0} \\ &\Leftrightarrow \quad \mathbf{K}^* d\mathbf{u}^* + d\lambda \mathbf{F}^* = -\mathbf{r}^*, \end{aligned} \tag{26}$$

where

$$\mathbf{K}^* = \begin{bmatrix} \mathbf{K} & -\mathbf{T}^T & \mathbf{0} \\ -\mathbf{T} & \mathbf{0} & \mathbf{L}_{22} \\ \mathbf{0} & \mathbf{L}_{22}^T & \mathbf{0} \end{bmatrix}, \quad \mathbf{F}^* = \begin{bmatrix} \mathbf{0} \\ \mathbf{L}_{11} \\ 0 \end{bmatrix}, \tag{27}$$

and $\mathbf{K} = \frac{\partial \mathbf{r_u}}{\partial \mathbf{u}}$. To solve (26), we employ the MGDCM, cf. Leon et al. [33].

PDE filter of volume fraction field

Stationarity of (12) requires (ν, μ) to satisfy

$$\begin{aligned}\delta\Pi(\nu,\mu;\delta\nu,\delta\mu) = \quad & \int_\Omega l^2 \boldsymbol{\nabla}\nu\boldsymbol{\nabla}\delta\nu \, dV - \int_\Omega (\nu - z)\delta\nu \, dV + \sum_{j=1}^{2} \int_{\partial\Omega^{j+}} \delta\mu(\nu - \nu(\boldsymbol{X} - \boldsymbol{A}_j)) \, dS \\ & + \sum_{j=1}^{2} \int_{\partial\Omega^{j+}} \mu(\delta\nu - \delta\nu(\boldsymbol{X} - \boldsymbol{A}_j)) \, dS = 0,\end{aligned} \tag{28}$$

for all admissible $(\delta\nu, \delta\mu)$. To solve (28), we parameterize z via the piece-wise uniform design field $\mathsf{z} : \Omega^r \to [0,1]$ over the finite elements $\Omega^e \in \Omega$, such that $z(\boldsymbol{X}) = \mathsf{z}_e$ for $\boldsymbol{X} \in \Omega^r_e$. The filtered field ν, is interpolated via linear shape functions through the nodal filtered density degrees-of-freedom vector $\boldsymbol{\nu}$. We again enforce the periodicity constraints nodal-wise, and agglomerate the Lagrange multipliers in the vector $\boldsymbol{\mu} \in \mathbb{R}^m$. Using the arbitrariness of $\delta\nu$ and $\delta\mu$, the discretized version of (28) is

$$\begin{bmatrix} l_o^2\mathbf{K}_\nu + \mathbf{M}_\nu & \mathbf{T}_\nu^T \\ \mathbf{T}_\nu & \mathbf{0} \end{bmatrix} \begin{bmatrix} \boldsymbol{\nu} \\ \boldsymbol{\mu} \end{bmatrix} = \begin{bmatrix} \mathbf{P}_\nu \mathbf{z} \\ \mathbf{0} \end{bmatrix} \quad \Leftrightarrow \quad \mathbf{K}^*_\nu \boldsymbol{\nu}^* = \mathbf{P}^*_\nu \mathbf{z}^*, \tag{29}$$

where the explicit forms of $\mathbf{K}_\nu$, $\mathbf{M}_\nu$ and $\mathbf{P}_\nu$ appear in Lazarov and Sigmund [31], and $\mathbf{T}_\nu$ is analogous to $\mathbf{T}$.

PDE filter of shape displacement field

Stationarity of (19) requires $(\boldsymbol{\psi}, \boldsymbol{\Upsilon})$ to satisfy

$$\begin{aligned}\delta\Gamma(\boldsymbol{\psi},\boldsymbol{\Upsilon};\delta\boldsymbol{\psi},\delta\boldsymbol{\Upsilon}) = \quad & \int_{\Omega_o} \boldsymbol{P}_\psi : \boldsymbol{\nabla}\delta\boldsymbol{\psi} \, dV + \int_{\partial\Omega^d_o} \delta\boldsymbol{\psi}(\boldsymbol{X}_o) \cdot (\boldsymbol{\psi}(\boldsymbol{X}_o) - \lambda_d \boldsymbol{d}(\boldsymbol{X}_o)) \, dS \\ & + \sum_{j=1}^{2} \int_{\partial\Omega^{j+}} \delta\boldsymbol{\Upsilon}(\boldsymbol{X}_o) \cdot (\boldsymbol{\psi}(\boldsymbol{X}_o) - \boldsymbol{\psi}(\boldsymbol{X}_o - \boldsymbol{A}_j)) \, dS \\ & + \sum_{j=1}^{2} \int_{\partial\Omega^{j+}} \boldsymbol{\Upsilon}(\boldsymbol{X}_o) \cdot (\delta\boldsymbol{\psi}(\boldsymbol{X}_o) - \delta\boldsymbol{\psi}(\boldsymbol{X}_o - \boldsymbol{A}_j)) \, dS = 0,\end{aligned} \tag{30}$$

for all admissible $(\delta\boldsymbol{\psi}, \delta\boldsymbol{\Upsilon})$. In the above, $\boldsymbol{P}_\psi = \frac{\partial W_\psi}{\partial \boldsymbol{\nabla}\boldsymbol{\psi}}$. To solve (30), we interpolate $\boldsymbol{d}$ and $\boldsymbol{\psi}$ via quadratic shape functions and the nodal displacement vectors $\mathbf{d}$ and $\boldsymbol{\psi}$. We again enforce the periodicity constraints nodal-wise, and agglomerate the Lagrange multipliers in the vector $\boldsymbol{\Upsilon} \in \mathbb{R}^{2m}$. The discretized version of (30) is

$$\delta\boldsymbol{\psi}^T \left(\sum\!\!\!\!\!\!\int_{\Omega_o} \boldsymbol{\nabla}\mathbf{N}^T \mathbf{P}_\psi \, dV + \sum\!\!\!\!\!\!\int_{\partial\Omega^d_o} \mathbf{N}^T (\boldsymbol{\psi} - \lambda_d \boldsymbol{d}) \, dS + \mathbf{T}^T \boldsymbol{\Upsilon} \right) + \delta\boldsymbol{\Upsilon}^T \mathbf{T}\boldsymbol{\psi} = 0. \tag{31}$$

Using the arbitrariness of $\delta\boldsymbol{\psi}$ and $\delta\boldsymbol{\Upsilon}$ in (31), we obtain

$$\mathbf{r}^*_{\boldsymbol{\psi}}(\boldsymbol{\psi}^*) = \begin{bmatrix} \mathbf{r}_{\boldsymbol{\psi}} \\ \mathbf{r}_{\boldsymbol{\Upsilon}} \end{bmatrix} = \mathbf{0}, \tag{32}$$

where $\boldsymbol{\psi}^* = [\boldsymbol{\psi},\ \boldsymbol{\Upsilon}]^T$, $\mathbf{r}_{\boldsymbol{\psi}} = \sum\sum \int_{\Omega_o} \boldsymbol{\nabla}\mathbf{N}^T\mathbf{P}_{\psi}\, dV + \sum\sum \int_{\partial\Omega_o^d} \mathbf{N}^T\left(\boldsymbol{\psi} - \lambda_d \boldsymbol{d}\right)\, dS + \mathbf{T}^T\boldsymbol{\Upsilon}$ and $\mathbf{r}_{\boldsymbol{\Upsilon}} = \mathbf{T}\boldsymbol{\psi}$. We utilize Newton's method to find the $\boldsymbol{\psi}^*$ which fulfills (32), i.e. we prescribe a λ_d and linearize

$$\mathbf{r}^*_{\boldsymbol{\psi}}(\boldsymbol{\psi}^* + \delta\boldsymbol{\psi}^*) \approx \mathbf{r}^*_{\boldsymbol{\psi}} + \frac{\partial \mathbf{r}^*_{\boldsymbol{\psi}}}{\partial \boldsymbol{\psi}^*} d\boldsymbol{\psi}^* = \mathbf{0}, \quad \Leftrightarrow \quad \mathbf{K}^*_{\boldsymbol{\psi}} d\mathbf{r}^*_{\boldsymbol{\psi}} = -\mathbf{r}^*_{\boldsymbol{\psi}}, \tag{33}$$

where

$$\mathbf{K}^*_{\boldsymbol{\psi}} d\boldsymbol{\psi}^* = \begin{bmatrix} \mathbf{K}_{\boldsymbol{\psi}} & \mathbf{T}^T \\ \mathbf{T} & \mathbf{0} \end{bmatrix} \begin{bmatrix} d\boldsymbol{\psi} \\ d\boldsymbol{\Upsilon} \end{bmatrix}, \tag{34}$$

and $\mathbf{K}_{\boldsymbol{\psi}} = \frac{\partial \mathbf{r}_{\boldsymbol{\Psi}}}{\partial \boldsymbol{\psi}}$.

Sensitivity analysis

We use the $(\,\cdot\,)_f$ notations for all quantities associated with the filter problems and let $\boldsymbol{\rho}$ denote the design variables. In the adjoint method, we augment the function $g = g(\mathbf{u}^*(\boldsymbol{\rho}_f(\boldsymbol{\rho})))$ with the equality constraints, i.e. residuals, for the state $\mathbf{r}^*$ and filter $\mathbf{r}_f$ problems, such that

$$\hat{g} = g - \boldsymbol{\lambda}^{*,T}\mathbf{r}^* - \boldsymbol{\lambda}_f^T\mathbf{r}_f, \tag{35}$$

where $\boldsymbol{\lambda}^*$ and $\boldsymbol{\lambda}_f$ are adjoint vectors. Differentiation of (35) with respect to the design variables yields

$$\frac{\partial \hat{g}}{\partial \boldsymbol{\rho}} = -\boldsymbol{\lambda}_f^T \frac{\partial \mathbf{r}_f}{\partial \boldsymbol{\rho}} + \left(\left(\frac{\partial g}{\partial \mathbf{u}^*} - \boldsymbol{\lambda}^{*,T} \frac{\partial \mathbf{r}^*}{\partial \mathbf{u}^*} \right) \frac{\partial \mathbf{u}^*}{\partial \boldsymbol{\rho}_f} - \boldsymbol{\lambda}^{*,T} \frac{\partial \mathbf{r}^*}{\partial \boldsymbol{\rho}_f} - \boldsymbol{\lambda}_f^T \frac{\partial \mathbf{r}_f}{\partial \boldsymbol{\rho}_f} \right) \frac{\partial \boldsymbol{\rho}_f}{\partial \boldsymbol{\rho}}. \tag{36}$$

Now, we solve the coupled system below for the adjoint vectors

$$\begin{aligned} \frac{\partial \mathbf{r}^*}{\partial \mathbf{u}^*}\boldsymbol{\lambda}^* &= \left(\frac{\partial g}{\partial \mathbf{u}^*} \right)^T, \\ \frac{\partial \mathbf{r}_f}{\partial \boldsymbol{\rho}_f}\boldsymbol{\lambda}_f &= -\left(\frac{\partial \mathbf{r}^*}{\partial \boldsymbol{\rho}_f} \right)^T \boldsymbol{\lambda}^*, \end{aligned} \tag{37}$$

to annihilate the implicit sensitivities $\frac{\partial \mathbf{u}^*}{\partial \boldsymbol{\rho}_f}$ and $\frac{\partial \boldsymbol{\rho}_f}{\partial \boldsymbol{\rho}}$ in (37). We emphasize that $\mathbf{K}^* = \frac{\partial \mathbf{r}^*}{\partial \mathbf{u}^*}$ appears in (27). Depending on whether it is the topology or shape sensitivities that are sought, $\frac{\partial \mathbf{r}_f}{\partial \boldsymbol{\rho}_f}$ appears in (29) or (34). What remains of (36) is

$$\frac{\partial \hat{g}}{\partial \boldsymbol{\rho}} = -\boldsymbol{\lambda}_f^T \frac{\partial \mathbf{r}_f}{\partial \boldsymbol{\rho}}, \tag{38}$$

which is the sensitivity of $\hat{g} = g$. We find $\frac{\partial \mathbf{r}_f}{\partial \boldsymbol{\rho}} = \mathbf{P}^*_{\nu}$ via (29) or $\frac{\partial \mathbf{r}_f}{\partial \boldsymbol{\rho}} = \begin{bmatrix} -\sum\sum \int_{\partial\Omega_o^d} \lambda_d \mathbf{N}^T\mathbf{N}\, dS & \mathbf{0} \end{bmatrix}^T$ via (32) if conducting topology or shape optimization, respectively.

Now, specializing the (37) result to the objective function (17), we find

$$\left(\frac{\partial g_o}{\partial \mathbf{u}^*}\right)^T = \begin{bmatrix} \mathbf{0} \\ \displaystyle\sum_{j=1}^{N_p} 2\omega^j \left(\frac{1}{|\Omega| F_{22}^{M,j}} \mathbf{L}_{11}^T \mathbf{\Lambda}^j - \bar{\sigma}^{M,j}\right) \frac{1}{|\Omega| F_{22}^{M,j}} \mathbf{L}_{11} \\ \displaystyle\sum_{j=1}^{N_p} 2\omega^j \left(\frac{1}{|\Omega| F_{22}^{M,j}} \mathbf{L}_{11}^T \mathbf{\Lambda}^j - \bar{\sigma}^{M,j}\right) \frac{1}{|\Omega|} \mathbf{L}_{11}^T \mathbf{\Lambda}^j \left(\frac{-1}{\left(F_{22}^{M,j}\right)^2}\right) \end{bmatrix}. \tag{39}$$

In the topology optimization, $\left(\frac{\partial \mathbf{r}^*}{\partial \boldsymbol{\rho}_f}\right)^T = \left(\frac{\partial \mathbf{r}^*}{\partial \boldsymbol{\nu}}\right)^T$ is

$$\left(\frac{\partial \mathbf{r}^*}{\partial \boldsymbol{\nu}}\right)^T = \begin{bmatrix} \sum \left[\displaystyle\int_{\Omega^e} \boldsymbol{\nabla} \mathbf{N}^T \frac{\partial \mathbf{P}}{\partial \boldsymbol{\nu}^e} \, dV + \int_{\Omega^e} k_r \frac{\partial \mathcal{I}}{\partial \boldsymbol{\nu}^e} \mathbf{H}^T \mathbf{H} \mathbf{u}^e \, dV \right] \\ \mathbf{0} \\ 0 \end{bmatrix}, \tag{40}$$

which is readily evaluated using (13) and (16). In the shape optimization, $\left(\frac{\partial \mathbf{r}^*}{\partial \boldsymbol{\rho}_f}\right)^T = \left(\frac{\partial \mathbf{r}^*}{\partial \boldsymbol{\psi}}\right)^T$ is

$$\left(\frac{\partial \mathbf{r}^*}{\partial \boldsymbol{\psi}}\right)^T = \begin{bmatrix} \left(\frac{\partial \mathbf{r}_\mathbf{u}}{\partial \boldsymbol{\psi}}\right)^T \\ \mathbf{0} \\ 0 \end{bmatrix}, \tag{41}$$

where

$$\left(\frac{\partial \mathbf{r}_\mathbf{u}}{\partial \boldsymbol{\psi}}\right)^T = \sum \Bigg[\int_{\Omega^e} \left(\left(\frac{\partial \boldsymbol{\nabla} \mathbf{N}^T}{\partial \boldsymbol{\psi}^e} \mathbf{P} + \boldsymbol{\nabla} \mathbf{N}^T \frac{\partial \mathbf{P}}{\partial \mathbf{F}} \frac{\partial \boldsymbol{\nabla} \mathbf{N}}{\partial \boldsymbol{\psi}^e} \mathbf{u}^e \right) dV + \boldsymbol{\nabla} \mathbf{N}^T \mathbf{P} \frac{\partial dV}{\partial \boldsymbol{\psi}^e} \right) + \int_{\Omega^e} k_r \mathcal{I} \left(2 \frac{\partial \mathbf{H}^T}{\partial \boldsymbol{\psi}^e} \mathbf{H} \mathbf{u}^e \, dV + \mathbf{H}^T \mathbf{H} \mathbf{u}^e \frac{\partial dV}{\partial \boldsymbol{\psi}^e} \right) \Bigg]. \tag{42}$$

To find $\frac{\partial \mathbf{H}}{\partial \boldsymbol{\psi}^e}$, we use (24), i.e.

$$\frac{\partial \boldsymbol{M}}{\partial \boldsymbol{\psi}^e} \boldsymbol{y} + \boldsymbol{M} \frac{\partial \boldsymbol{y}}{\partial \boldsymbol{\psi}^e} = \frac{\partial \boldsymbol{b}}{\partial \boldsymbol{\psi}^e} \quad \Leftrightarrow \quad \boldsymbol{M} \frac{\partial \boldsymbol{y}}{\partial \boldsymbol{\psi}^e} = \frac{\partial \boldsymbol{b}}{\partial \boldsymbol{\psi}^e} - \frac{\partial \boldsymbol{M}}{\partial \boldsymbol{\psi}^e} \boldsymbol{y}. \tag{43}$$

Solving the above for $\frac{\partial \boldsymbol{y}}{\partial \boldsymbol{\psi}^e}$ yields the terms of $\frac{\partial \mathbf{H}}{\partial \boldsymbol{\psi}^e}$. The remaining shape sensitivities $\frac{\partial \boldsymbol{\nabla} \mathbf{N}}{\partial \boldsymbol{\psi}^e}$ and $\frac{\partial dV}{\partial \boldsymbol{\psi}^e}$ appear in Haslinger and Mäkinen [25].

Appendix B

Supplementary material related to this article can be found online at LINK TO FIGS.

Declaration of Competing Interests

The authors declare that they have no competing interest.

References

[1] Alberdi, R., Khandelwal, K., 2019. Design of periodic elastoplastic energy dissipating microstructures. Structural and Multidisciplinary Optimization 59, 461–483.

[2] Amstutz, S., Van Goethem, N., 2012. Topology optimization methods with gradient-free perimeter approximation. Interfaces and Free Boundaries 14, 401–430.

[3] Bendsøe, M.P., 1989. Optimal shape design as a material distribution problem. Structural optimization 1, 193–202.

[4] Bertoldi, K., Boyce, M., 2008. Mechanically triggered transformations of phononic band gaps in periodic elastomeric structures. Physical Review B 77, 052105.

[5] Bletzinger, K.U., 2014. A consistent frame for sensitivity filtering and the vertex assigned morphing of optimal shape. Structural and Multidisciplinary Optimization 49, 873–895.

[6] Bluhm, G.L., 2021. Analysis and optimization of nonlinear structures and materials including internal contact. Technical University of Denmark.

[7] Bluhm, G.L., Sigmund, O., Poulios, K., 2021. Internal contact modeling for finite strain topology optimization. Computational Mechanics 67, 1099–1114.

[8] Bluhm, G.L., Sigmund, O., Wang, F., Poulios, K., 2020. Nonlinear compressive stability of hyperelastic 2d lattices at finite volume fractions. Journal of the Mechanics and Physics of Solids 137, 103851.

[9] Bog, T., Zander, N., Kollmannsberger, S., Rank, E., 2015. Normal contact with high order finite elements and a fictitious contact material. Computers & Mathematics with Applications 70, 1370–1390.

[10] Bruns, T.E., Tortorelli, D.A., 2001. Topology optimization of non-linear elastic structures and compliant mechanisms. Computer methods in applied mechanics and engineering 190, 3443–3459.

[11] Chen, Q., Zhang, X., Zhu, B., 2018. Design of buckling-induced mechanical metamaterials for energy absorption using topology optimization. Structural and Multidisciplinary Optimization 58, 1395–1410.

[12] Chenais, D., 1975. On the existence of a solution in a domain identification problem. Journal of Mathematical Analysis and Applications 52, 189–219.

[13] Christiansen, R.E., Sigmund, O., 2016. Designing meta material slabs exhibiting negative refraction using topology optimization. Structural and Multidisciplinary Optimization 54, 469–482.

[14] Clausen, A., Wang, F., Jensen, J.S., Sigmund, O., Lewis, J.A., 2015. Topology optimized architectures with programmable poisson's ratio over large deformations. Adv. Mater 27, 5523–5527.

[15] Coulais, C., Sabbadini, A., Vink, F., van Hecke, M., 2018. Multi-step self-guided pathways for shape-changing metamaterials. Nature 561, 512–515.

[16] Crisfield, M.A., 1993. Non-linear finite element analysis of solids and structures. volume 1. Wiley.

[17] Dalklint, A., Wallin, M., Bertoldi, K., Tortorelli, D., 2022. Tunable phononic bandgap materials designed via topology optimization. Journal of the Mechanics and Physics of Solids 163, 104849.

[18] Danielsson, M., Parks, D., Boyce, M., 2002. Three-dimensional micromechanical modeling of voided polymeric materials. Journal of the Mechanics and Physics of Solids 50, 351–379.

[19] De Souza Neto, E.A., Blanco, P.J., Sánchez, P.J., Feijóo, R.A., 2015. An rve-based multiscale theory of solids with micro-scale inertia and body force effects. Mechanics of Materials 80, 136–144.

[20] Deng, H., Cheng, L., Liang, X., Hayduke, D., To, A.C., 2020. Topology optimization for energy dissipation design of lattice structures through snap-through behavior. Computer Methods in Applied Mechanics and Engineering 358, 112641.

[21] Evans, K.E., Alderson, A., 2000. Auxetic materials: functional materials and structures from lateral thinking! Advanced materials 12, 617–628.

[22] Fernandez, F., Puso, M.A., Solberg, J., Tortorelli, D.A., 2020. Topology optimization of multiple deformable bodies in contact with large deformations. Computer Methods in Applied Mechanics and Engineering 371, 113288.

[23] Guest, J.K., Prévost, J.H., Belytschko, T., 2004. Achieving minimum length scale in topology optimization using nodal design variables and projection functions. International journal for numerical methods in engineering 61, 238–254.

[24] Haber, R.B., Jog, C.S., Bendsøe, M.P., 1996. A new approach to variable-topology shape design using a constraint on perimeter. Structural optimization 11, 1–12.

[25] Haslinger, J., Mäkinen, R.A., 2003. Introduction to shape optimization: theory, approximation, and computation. SIAM.

[26] Hill, R., 1972. On constitutive macro-variables for heterogeneous solids at finite strain. Proceedings of the Royal Society of London. A. Mathematical and Physical Sciences 326, 131–147.

[27] Ivarsson, N., Wallin, M., Tortorelli, D.A., 2020. Topology optimization for designing periodic microstructures based on finite strain viscoplasticity. Structural and Multidisciplinary Optimization 61, 2501–2521.

[28] Kruse, R., Nguyen-Thanh, N., Wriggers, P., De Lorenzis, L., 2018. Isogeometric frictionless contact analysis with the third medium method. Computational Mechanics 62, 1009–1021.

[29] Lakes, R., 1987. Foam structures with a negative poisson's ratio. Science 235, 1038–1040.

[30] Lakes, R., 2007. Cellular solids with tunable positive or negative thermal expansion of unbounded magnitude. Applied physics letters 90, 221905.

[31] Lazarov, B.S., Sigmund, O., 2011. Filters in topology optimization based on helmholtz-type differential equations. International Journal for Numerical Methods in Engineering 86, 765–781.

[32] Le, C., Bruns, T., Tortorelli, D., 2011. A gradient-based, parameter-free approach to shape optimization. Computer Methods in Applied Mechanics and Engineering 200, 985–996.

[33] Leon, S.E., Lages, E.N., De Araújo, C.N., Paulino, G.H., 2014. On the effect of constraint parameters on the generalized displacement control method. Mechanics Research Communications 56, 123–129.

[34] Mandel, J., 1971. Plasticité classique et viscoplasticité (cism lecture notes, udine, italy).

[35] Saeb, S., Steinmann, P., Javili, A., 2016. Aspects of computational homogenization at finite deformations: a unifying review from reuss' to voigt's bound. Applied Mechanics Reviews 68.

[36] Scherer, M., Denzer, R., Steinmann, P., 2010. A fictitious energy approach for shape optimization. International Journal for Numerical Methods in Engineering 82, 269–302.

[37] Sigmund, O., 1997. On the design of compliant mechanisms using topology optimization. Journal of Structural Mechanics 25, 493–524.

[38] Sigmund, O., Jensen, J.S., 2003. Systematic design of phononic band–gap materials and structures by topology optimization. Philosophical Transactions of the Royal Society of London. Series A: Mathematical, Physical and Engineering Sciences 361, 1001–1019.

[39] Sigmund, O., Petersson, J., 1998. Numerical instabilities in topology optimization: a survey on procedures dealing with checkerboards, mesh-dependencies and local minima. Structural optimization 16, 68–75.

[40] Sigmund, O., Torquato, S., 1996. Composites with extremal thermal expansion coefficients. Applied Physics Letters 69, 3203–3205.

[41] Stolpe, M., Svanberg, K., 2001. An alternative interpolation scheme for minimum compliance topology optimization. Structural and Multidisciplinary Optimization 22, 116–124.

[42] Strömberg, N., Klarbring, A., 2010. Topology optimization of structures in unilateral contact. Structural and Multidisciplinary Optimization 41, 57–64.

[43] Svanberg, K., 1987. The method of moving asymptotes-a new method for structural optimization. International journal for numerical methods in engineering 24, 359–373.

[44] Swartz, K., Mittal, K., Schmidt, M., Barrera, J., Watts, S., Tortorelli, D., 2023. Yet another parameter-free shape optimization method .

[45] Swartz, K.E., Tortorelli, D.A., White, D.A., James, K.A., 2022. Manufacturing and stiffness constraints for topology optimized periodic structures. Structural and Multidisciplinary Optimization 65, 1–20.

[46] Swartz, K.E., White, D.A., Tortorelli, D.A., James, K.A., 2021. Topology optimization of 3d photonic crystals with complete bandgaps. Optics Express 29, 22170–22191.

[47] Valentine, J., Zhang, S., Zentgraf, T., Ulin-Avila, E., Genov, D.A., Bartal, G., Zhang, X., 2008. Three-dimensional optical metamaterial with a negative refractive index. nature 455, 376–379.

[48] Villanueva, C.H., Maute, K., 2014. Density and level set-xfem schemes for topology optimization of 3-d structures. Computational Mechanics 54, 133–150.

[49] Wagner, M., Schwarz, F., Huber, N., Geistlich, L., Galinski, H., Spolenak, R., 2021. Deformation-induced topological transitions in mechanical metamaterials and their application to tunable non-linear stiffening. arXiv preprint arXiv:2111.05284 .

[50] Wallin, M., Ivarsson, N., Amir, O., Tortorelli, D., 2020. Consistent boundary conditions for pde filter regularization in topology optimization. Structural and Multidisciplinary Optimization .

[51] Wallin, M., Tortorelli, D.A., 2020. Nonlinear homogenization for topology optimization. Mechanics of Materials 145, 103324.

[52] Wang, F., 2018. Systematic design of 3d auxetic lattice materials with programmable poisson's ratio for finite strains. Journal of the Mechanics and Physics of Solids 114, 303–318.

[53] Wang, F., Lazarov, B.S., Sigmund, O., Jensen, J.S., 2014a. Interpolation scheme for fictitious domain techniques and topology optimization of finite strain elastic problems. Computer Methods in Applied Mechanics and Engineering 276, 453–472.

[54] Wang, F., Sigmund, O., Jensen, J.S., 2014b. Design of materials with prescribed nonlinear properties. Journal of the Mechanics and Physics of Solids 69, 156–174.

[55] Wang, P., Casadei, F., Shan, S., Weaver, J.C., Bertoldi, K., 2014c. Harnessing buckling to design tunable locally resonant acoustic metamaterials. Physical review letters 113, 014301.

[56] Wang, Q., Jackson, J.A., Ge, Q., Hopkins, J.B., Spadaccini, C.M., Fang, N.X., 2016. Lightweight mechanical metamaterials with tunable negative thermal expansion. Physical review letters 117, 175901.

[57] Wriggers, P., Schröder, J., Schwarz, A., 2013. A finite element method for contact using a third medium. Computational Mechanics 52, 837–847.

[58] Zhang, G., Feng, N., Khandelwal, K., 2021. A computational framework for homogenization and multiscale stability analyses of nonlinear periodic materials. International Journal for Numerical Methods in Engineering 122, 6527–6575.

[59] Zhang, G., Khandelwal, K., 2020. Topology optimization of dissipative metamaterials at finite strains based on nonlinear homogenization. Structural and Multidisciplinary Optimization 62, 1419–1455.

[60] Zhang, S., Fan, W., Panoiu, N., Malloy, K., Osgood, R., Brueck, S., 2005. Experimental demonstration of near-infrared negative-index metamaterials. Physical review letters 95, 137404.

[61] Zienkiewicz, O., Campbell, J., 1973. Shape optimization and sequential linear programming. In Optimum Structural Design, Gallagher R, Zienkiewicz OC (Eds.) , 109–126.